On synchronization of life cycles by collective transport and emergence of supercycles

Sergei Esipov[1] and Clara Salueña[2]
[1] *Quant Isle Ltd., Scarsdale, New York, USA*
[2] *Departament d'Enginyeria Mecànica, Universitat Rovira i Virgili, 43007 Tarragona, Spain*
(Dated: November 10, 2021)

A model of physiological age, accompanied by non-linear diffusion in space, is studied analytically and numerically, and is shown to develop non-stationary traveling population waves. A window of intermediate growth rates is found where collective supercycles are formed from individual (stochastic) life cycles. Supercycle periods can be considerably different (larger or smaller) than the average longevities of contributing individuals, while the time-averaged spatial expansion rate has a local maximum in the supercycling mode. A method of adiabatic similarity solutions is used to derive dependencies of the solution parameters on source and sink inhomogeneities, and obtain closed coupled dynamic equations for the age structure, leading and trailing fronts. Analytical results are compared with numerically computed similarity and full solutions for several types of population waves. We discuss possible model applications to development of lichen thallus, multi-year patterns of agricultural crop yields and autocorrelation of locust swarming.

PACS numbers: 87.10.Ed, 87.18.Hf, 87.23.Cc, 05.65.+b, 05.40.-a

I. INTRODUCTION

Spontaneously synchronized oscillations in mixtures of organic molecules are currently hypothesized to be a precursor of life [1, 2]. At different levels of biological aggregation, be it cells, cellular organisms, or groups of organisms, one finds examples of recurrent cycles –which are not necessarily strictly periodic but exhibit considerable cycle elasticity. Historical data exist in the literature for some of these cycles. We will confine ourselves with three examples below. Lichen colonies of *Parmelia conspersa* may display periodic thallus growth with a period of several weeks [3]. Many agricultural yields display striking multi-year patterns [4, 5]. Swarming of locusts in Eastern Australia [6], although not at all periodic, displays significant autocorrelation with peak-to-peak lags of several years, despite all the control efforts.

In the absence of any obvious external drivers or internal "dedicated clocks", these cycles suggest flexible inter-organism regulation, and the key question is - how does a recurrent behavior emerge from the lower scale life-cycles of the involved organisms or cells, a behavior which is clearly robust while being different from these lower-level variable life-cycles?

We use the term "cells" here to refer to individual live agents, which could literally be independent motile cells, such as bacteria, but could also entirely depend on hosts for transport as viruses do [20, 21], or to be multicellular organisms, such as swarming insects [22] or plants and their fruits, exhibiting cycles [4]. Synchronization by collective transport is characteristic of relatively early stages of collective organization, when cell density is small as compared to close packing.

Here we analyze theoretically a model of collective cell behavior and pattern formation on time scales not reducible to the duration of individual life cycles. There are, in principle, several approaches at hand. First, collective and self-organized motion of interacting agents in swarms, and flocking mechanisms are often described micro- and mesoscopically by means of particle or agent-based models [7]. These models can satisfactorily account for different aspects of the aggregated motion of elementary agents, but none of them, to our knowledge, contemplates the emergence of temporal supercycles from steady-moving waves. Periodic traveling population waves can be modeled via two-species reaction-diffusion systems of equations [8], which are capable, as in chemically reactive species, to account for cyclic spatio-temporal patterns characterized by population synchronicities across the spatial domain. However, there is no net propagation of individuals in these waves, limiting their biological applications. A different class of models is based on the generalization of the Kolmogorov-Petrovsky-Piskunov-Fisher (KPPF) equation [9, 10], a type of reaction-diffusion equation which produces steady state patterns after inclusion of non-local competition terms, both with linear and non-linear diffusion [11, 12]. Beyond pure random motion, the chosen form of non-linear diffusion may boost (superdiffusion), or hinder (subdiffusion) individual displacements depending on the local population density, favoring the mobility of some cohorts with respect to others, to avoid or enhance crowding. Non-linear diffusion plays an important role in spatially inhomogeneous population dynamics [13] and has been used to model insect dispersal [14] and bacterial chemotaxis [15]. Here we will show theoretically how, combined with a non-local functional dependence plus physiological aging variability, non-linear diffusion may give rise to a rich phenomenology, which includes self-organized swarming aging structures.

In what follows we will use the notion of *physiological age* of individual cells or organisms as a measure of the phase or stage of the individual life cycle. This age was introduced by VanSickle as "some measure of maturity or physiological development of individuals in a population ... [such as] chronological age, body size, chemical

composition or any other physiological feature which is an accurate indicator of an individuals reproductive status and potential for survival" [16]. VanSickle considered a deterministic physiological age which had its own accumulation rate. The chronological age was recovered if the growth rate is 1. In VanSickle's approach, a distribution of deterministic physiological rates encounters a problem with multiple stages or development: with a deterministic rate one can predict the timing of the future stages, including death, based upon the time it took to achieve past stages.

We have previously studied the variability of physiological age in a stochastic setting. An age-resolved population dynamics in space and time was introduced for *Proteus mirabilis* [17]. This paper contained analysis of a model where variable age-resolved population is described by an integro-differential equation. The model bore mathematical similarities to the Boltzmann kinetic equation in the theory of ideal gases, and was termed "kinetic". A corresponding minimal model without integral terms, and with potentially broader applicability, was presented in [18], where the diffusion (Fokker-Planck) approximation was introduced along the age axis for age-structured populations. The present paper contains a quantitative study of pulsating waves or "supercycles" in the diffusion approximation along the age axis, and discusses its potential applications.

To aid with the analytical study, we use a method of parametrically driven similarity solutions, based on their stability [19]. In this method, the evolution under the influence of slow external changes in the population is projected on similarity solutions with adiabatically updated parameters.

II. THE MODEL

A multicellular organism controls birth, development and apoptosis of individual cells. This is a flexible control which, to some extent, has to tolerate individual advances and delays of cell development. Groups of cells forming internal structural elements may pass through different development phases at different times. For modeling purposes we assume that each element, be it a cell, or a group of cells (we call these elements *cells* until noted otherwise), has a life trajectory which can be parameterized quantitatively by the physiological age θ. The properties of this variable are as follows. When an observer is presented with a group of individuals born at the same time, she may conclude that the individuals appear to be at somewhat different physiological stages, and continue to mature differently at any chronological age. For example, the onset of flowering in a grove may vary by several days [23] depending on the tree, or even vary by several weeks, depending on the species [24].

A. Physiological stages

In discrete time setting, $t/\Delta t = 0, 1, 2...$, the physiological age θ_t advances as

$$\theta_{t+\Delta t} = \theta_t + a_0 + a_1 z, \tag{1}$$

where a_0, $a_1 > 0$ are constants and z is a Bernoulli variable, having values 1 and 0 with probabilities p and $1-p$, respectively. If time step Δt is sufficiently small for a given time t, the limit of this process, is a sum of drift and diffusion, $\theta_t = (a_0+a_1p)(t/\Delta t)+a_1 Z\left[p(1-p)(t/\Delta t)\right]^{1/2}$, where Z is a standard normal random variable. Since the scale of physiological age θ is arbitrary at this point, we may adjust it by dividing over $(a_0 + a_1p)/\Delta t$ so that the average advance of the parameter is the same as that of the chronological time. As for the adjusted variability, in the continuous limit, it comes from a diffusion term with diffusivity $a = a_1^2 p(1-p)/[2\Delta t(a_0 + a_1p)^2]$.

The variability of physiological aging grows here as a square-root of time, based on linear diffusion of θ. This is closer to observations than VanSickle's distributed deterministic physiological aging where deviations grow linearly in time, see e.g. Figure 1 and Table 1 (for age groups less than 60 years old) in [25]. The diffusivity, a, has units of time. For example, in olive orchards, the physiological age diffusion "length", $(2at)^{1/2}$, reaches about a week, over 250 days (to account for winter dormancy), $\sqrt{2 \times a \times 250} = 7$ gives a of about one tenth of a day.

With insects, such as the South American locust *Schistocerca cancellata*, in controlled laboratory conditions, the duration of adult female and male stages were measured to be 87 ± 35 and 90 ± 27 days, respectively [26]. This gives much larger age diffusivity values of $a \sim 7$ days for female and $a \sim 4$ days for male stages.

In the continuous setting, a modeled cell with physiological age θ and spatial coordinate x will proceed as

$$d\theta = dt + \sqrt{2a}\, dW_1, \tag{2}$$

$$dx = \sqrt{2D}\, dW_2, \tag{3}$$

where D is spatial diffusivity, and $W_{1,2}$ are corresponding Wiener processes. The Fokker-Planck equation for the probability of a cell having a given age θ at x is [27]

$$\frac{\partial P}{\partial t} + \frac{\partial P}{\partial \theta} = \frac{\partial}{\partial x}\left[D\frac{\partial P}{\partial x}\right] + \frac{\partial}{\partial \theta}\left[a\frac{\partial P}{\partial \theta}\right]. \tag{4}$$

The 2D-density of cells in (x, θ) is obtained by multiplying this probability P by the total number of cells.

B. Model equations

For modeling the propagating population front we have considered the following ingredients,

i. The underlying organization, at the cell level, is the cell cycle expectancy, θ_e, which comprises two alternating stages. These are the motile phase, and the non motile phase. They can also be named individual phase and collective phase. In this analysis, both phases are of equal duration, although other choices are possible.

ii. Physiological maturity is not a deterministic process but can be accelerated or delayed, according to the physiological age diffusivity a.

iii. The motile phase is characterized by nonzero spatial diffusivity. At age 0 cells are not motile. As they grow older and reach θ_0, they acquire the ability to spatially diffuse. The diffusion coefficient will depend non-linearly on cell density and its form fosters collective migration. If the total "cell" density is too high (cutoff n_0) cells freeze. When we speak about "rebirth", we mean a simple clock reset to $\theta = 0$, at which individual motility ceases. These choices are discussed more in detail below.

iv. Whether the individual cell dies physically or not after the motile, collective phase, is not the key issue. The key is that mobility ceases for these cells, their clock is reset, and we say that they "regain individuality". An example of this behavior at the cell level of organization is the Proteus mirabilis swarmers. At the ecological level, the locust outbreaks. Please note that neither cells nor insects die after their respective motile (or collective) phase ceases.

v. At any time, cells reproduce with Malthusian rate and their offspring inherit their age, which mostly implies their state, either individual or collective. While offspring born with the age of their parents may seem an awkward arctifact, think only that the age of offspring when unicellular organisms replicate is undefined. Moreover, in the *Proteus mirabilis* bacterial system, it has been shown that cell aggregates (swarmers), consisting of several nuclei, continue exponential growth of their bodies without septating. Locusts do not replicate like unicellular organisms either, but following instead a complex developmental process. However, *insects born within a gregarious phase group together as soon as they start to feed*. That means, they are not first isolated, randomly moving and feeding individuals (immobile phase) and later they become mobile locusts. Contrarily, nymphs born in the band stay and march within [30]. We may assume then, that locusts' offspring are born "locusts", because they move with the band as soon as eggs hatch, and need to feed themselves.

vi. We will be focusing on the properties of the population in the vicinity of a leading front, where abundance of "nutrient" is assumed. This is the case for early growth mechanisms, well represented by means of a Malthusian parameter, a simple but appropriate model which we will consider here. In standard microbiological tests for instance, many generations of cells can be supported before nutrients are exhausted. With this in mind, presently we will not account for cell mortality. Other growth dynamics, like the logistic model, might be considered, but under certain range of parameters the dynamics presented here will be recovered.

vii. Models in the literature sometimes require that a gradient in nutrient concentration (chemotaxis) promotes faster growth of the fronts [15] where cells have easier access to the nutrients, following the Keller-Segel model [31]. Under the assumption of unlimited access to nutrients at the propagating front, here we do not consider these effects.

viii. Last, we must bear in mind that this is a population model: none of the individual lives is represented by the model equation any better than the trajectory of one single water molecule is represented by the Navier Stokes equations.

Growth and diffusion are very elementary mechanisms. Growth is related to the need of expansion and colonizing new spaces, and isotropic diffusion –however non-linear and non-local, is the most general mechanism at hand to explore the new surroundings for whatever purpose: mating, feeding, dispersing seeds, or maturing and growing, that is, occupying previously empty spaces.

Consider Malthusian growth of a population in presence of variable physiological stages, "rebirth" (as a switching mechanism between them) and non-linear spatial diffusivity. Topologically, the physiological age θ, $0 \leq \theta \leq \theta_e$ is a transport process on a circle, $\mathbb{S}$, with average drift of aging accompanied by a natural variability around it [32]. The age θ-axis here is therefore proportional to the angle of cylindrical coordinates, the proportionality coefficient being the constant radius of the cylinder, $\theta_e/2\pi$. The collective transport in space is a process defined in $\mathbb{R}^d$, so in a one-dimensional setting, $-\infty < x < \infty$, the model is posed on a cylinder, $\mathbb{S} \times \mathbb{R}^1$, with time $t \geq 0$.

The model equation for the time evolution of the population density, $n(x, \theta, t)$ reads as follows,

$$\frac{\partial n}{\partial t} + \frac{\partial n}{\partial \theta} = \frac{\partial}{\partial x}\left[D(n)\frac{\partial n}{\partial x}\right] + a\frac{\partial^2 n}{\partial \theta^2} + \gamma n. \qquad (5)$$

The field n describes cells of a multicellular organism (such as a plant) whose parts have average life expectancy cell-cycle expectancy, θ_e and physiological variability a. Unless explicitly stated to the contrary, we will be working with a non-linear spatial diffusivity,

$$D(n, \theta) = D_0 f(\eta) H(\theta - \theta_0), \qquad (6)$$

with H being the Heaviside step function, and

$$\eta = \frac{1}{n_0}\int_{\theta_0}^{\theta_e} n d\theta, \quad f(\eta) = \begin{cases} \eta^m, & \eta < 1 \\ 0, & \eta \geq 1 \end{cases}, \qquad (7)$$

which favors collective migration or "quorum sensing". Here $m > 0$ and θ_0 is the age when cells acquire motility, $0 < \theta_0 < \theta_e$. The lower limit of the integral (7) may be set to a different value within the interval $[0, \theta_e]$, the results being qualitatively similar.

Our choice of spatial diffusion $D(n)$ priories two essential modeling elements,

1. The case where a density increase enhances diffusion, as in models of insect dispersal [14], where $D(n) = D_0(n/n_0)^m$ for an age-independent density n. Migration of insects is generally contingent on crowding [28]. Such nonlinear diffusion coefficient assumes that without insects there is no diffusion, implying a front profile that goes steeply to zero, with a divergent slope for $m > 1$, supported by experimental observations in bacterial colonies. Studies of locust swarms [29, 30] reveal that individuals at the leading front (where density is smaller than in the bulk) slow down and turn more often towards those behind. This behavior reduces their net displacement in comparison to the rest of the marching band (i.e. smaller diffusivity), serves to maintain cohesion, and creates a dense front.

2. The diffusivity cutoff in Eq. (6) set at a concentration n_0, is consistent with the objective of the nonlinear or collective transport to occupy new areas which are challenging for individuals. When this goal is accomplished, reproduction is attempted and spatial mobility is no longer favored. In other words, slowing down is associated with density and reproduction. Indeed, the internal regions of *Proteus mirabilis* colonies are immobile, while their concentration of cells is the highest [33]. Growth inside the central part of lichen colonies is arrested, see Sec.VI A. Mosquitoes, locusts, etc aggregate for ovipositioning, during which they do not migrate. Migratory birds move in flocks, which require a certain density. They have specialized habitats for breeding where they form dense colonies, and cease migration while breeding [34]. Notwithstanding the above, inside the colony, away from the leading front, at yet higher densities one might expect a density-dependent decline of reproduction [9, 10, 14] due to nutrient shortages, build-up of byproducts, etc. These processes are not considered here. Due to the diffusivity cutoff, the population beyond n_0 does not contribute to the spatial dynamics of the colony. We thus expect an active band of cells, contained in the spatial region where the diffusivity is nonzero: between the leading front, $x_0(t)$, defined by absence of cells ahead, and the trailing front, $x_1(t)$, where mobility ceases due to the diffusivity cutoff at $n = n_0$.

III. NUMERICAL SIMULATION

We first integrate Eqs. (5)-(6) numerically, in the (x, θ)–domain, using centered finite differences and explicit integration in time. A fifth order WENO scheme is used for the age advection term, to model sharp age profiles at vanishing age diffusivity when needed (for larger age diffusivities, a simple second order advection scheme is sufficient). The Courant number is 0.8. Spatial and age diffusion terms are handled by a second-order scheme. The grid is uniform in both directions, with step sizes Δx, $\Delta\theta$. To resolve cusps near the fronts one need small spatial steps, hence small time steps. The age axis, $0 \le \theta \le \theta_e$, is a ring, whereas the spatial domain has its upper limit set to a value well ahead of the leading front x_0 so that in simulation time it never interacts with the boundary. Due to the mobility cutoff n_0, the only portion of the population which is of interest here is that contained between the leading and the trailing fronts (see discussion in the previous section), i.e. inside the interval $x_1(t) \le x \le x_0(t)$. Initially, N_0 cells are born at time $t = 0$ uniformly in the interval, $x_1(0) = 0$, $x_0(0) = w_0$ and the initial distribution is such that the trailing front is $x_1(0) = 0$. With the explicit scheme, in addition to the CFL condition, both age and spatial diffusion limit the time step for stability, $\Delta t \le \min\left[(\Delta x)^2/4D_0,\ (\Delta\theta)^2/4a\right]$. Due to C^0 continuity, tracking of the moving front requires rather small step sizes Δx. This turns Eq.(5) into a stiff problem. Our MATLAB code is available to the reader as supplemental material [35].

Figure 1 shows representative trajectories of the leading and trailing fronts in time for two types of initial conditions (peaked and uniform) and different values of the growth parameter γ_0.

Slower growth rates γ_0 are shown in the left panel of Fig. 1, with the transition from linear growth ($\gamma_0 = 1$) to supercycles. At $\gamma_0 = 1$ the long-term asymptotic is linear growth. Oscillations of the peaked initial condition are only a transient, albeit a persistent one; the cells will eventually smooth out to a constant speed when peaked cells diffuse over the entire age axis, at times $t \approx \theta_e^2/a = 800$. At $\gamma_0 = 5$ the long-term asymptotic is supercycles, regardless of the initial condition. Higher growth rates γ_0 are shown in the right panel (note the change of the y-scale). In cases when supercycles are formed, one can see by counting the number of oscillations, that the cycle period depends on the growth rate, γ_0, and it is not equal to the life cycle span of individual cells ($\theta_e = 2$ is the same for all plots). The supercycle period may be lesser (left panel) or greater (right panel) than θ_e, depending on parameters. In particular, we show that for $\gamma_0 = 85$, the period is $T \approx 2.751\theta_e$, and for $\gamma_0 = 102$ is $\approx 5.22\theta_e$. One can also see a systematic decrease of relative durations of consolidation phases, although we chose the motility threshold to be in the middle of the age interval, $2\theta_0 = \theta_e$.

These numerical results suggest that different types of asymptotic solutions may be obtained, depending on

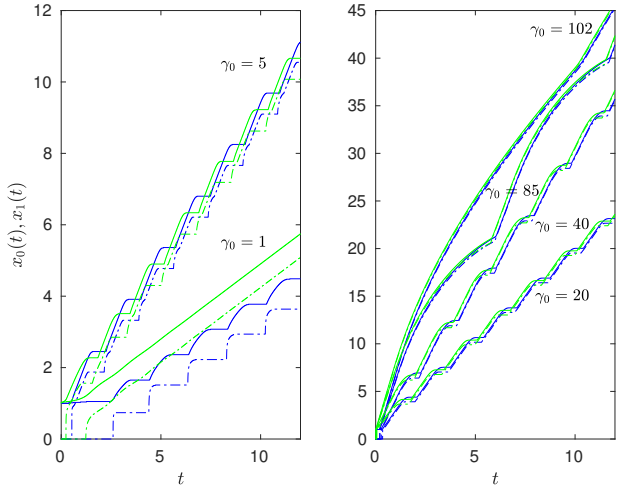

FIG. 1. Evolution of the leading (solid lines) and trailing (dashed lines) fronts depending on initial conditions and growth rates, as obtained by numerical integration of Eqs. (5)-(6). Parameters: $m = 4$, $\theta_0 = 1$, $\theta_e = 2$, $D_0 = 1$, $a = 0.005$, $w_0 = 1$, $n_0 = 1$. Blue lines correspond to a peaked initial condition $n(\theta, x, 0) = N_0\delta(\theta - \theta_0/2)$ (δ being the Dirac-δ function), with $N_0 = 10$, and $x \le w_0$. Green lines correspond to the uniform initial condition $n(\theta, x, 0) = N_0/\theta_0$, with $N_0 = 0.3$, and $x \le w_0$. In all cases $n(\theta, x, 0) = 0$ for $x > w_0$.

the parameters. In the case $\gamma_0 = 1$, the steady-moving fronts are faster than pulsating fronts. In other cases, the converse is true: even age-uniform initial conditions develop supercycles, and pulsating fronts advance faster than the steady-moving wave, in agreement with Saarloos marginal stability [36]. In the case $\gamma_0 = 5$ one can see additional inflection points on the front trajectories, hinting on different types of supercycles. Finally, if the growth rate, γ_0, is further increased, the period of supercycles increases until a linear growth in space is apparently recovered, see Sec. V.

We now introduce a method of parametrically driven similarity solutions, to obtain a closed system of ODEs for the propagating fronts. The reader not interested in theory and methodology may entirely dismiss Section IV.

In what follows, the 2D density $n(x, \theta, t)$ is referred to as "density", the 1D density $N(\theta, t) = \int n(x, \theta, t)dx$ is called age-density, and the 1D density $\mathfrak{n}(x, t) = \int n(x, \theta, t)d\theta$ is called concentration. The quantity $\mathfrak{N}(t) = \int n(x, \theta, t)dx$ denotes the total number of cells.

IV. PARAMETRICALLY DRIVEN SIMILARITY SOLUTIONS

The method presented here is valid when spatial transport is fast as compared to the source-sink terms.

A. Age-Independent Dynamics

Consider first the age-independent case, where there is no concentration cutoff for cell motility, no motility threshold, $\theta_0 = 0$, and no age diffusion, $a = 0$, so that the non-linear diffusivity Eq. (6) in this case is age-independent. We introduce, however, time-dependent growth rates $\gamma(t) > 0$. Integrating Eq. (5) over the θ-axis, we obtain

$$\mathfrak{n}(x, t) = \int_0^{\theta_e} n(x, t, \theta)d\theta, \quad \frac{\partial \mathfrak{n}}{\partial t} = \frac{\partial}{\partial x}\left[D(\mathfrak{n})\frac{\partial \mathfrak{n}}{\partial x}\right] + \gamma\mathfrak{n}, \tag{8}$$

With unrestricted non-linear diffusivity, this equation may be integrated for an arbitrary growth rate $\gamma(t)$ and the concentration profile $\mathfrak{n}(x, t)$, is given by a hull-shaped even function of x, with finite support, $|x| \le x_0(\tau)$, as derived in Appendix A,

$$\mathfrak{n}(x, t) = \frac{Ah(t)}{x_0(\tau)}\left[1 - \frac{x^2}{x_0^2(\tau)}\right]^{1/m}. \tag{9}$$

where A is an integration constant, and

$$\tau = \int_{t_0}^{t} h^m(t_1)dt_1, \quad \log h = \int_{t_0}^{t} \gamma(t_1)dt_1. \tag{10}$$

Here, t_0 is an arbitrary initial time, when the initial concentration profile has been forgotten. The point in space where $n = 0$ defines the *leading* front of the wave, $x_0(\tau)$, which satisfies the first order ODE (see Appendix for details)

$$\frac{x_0'}{x_0} = \frac{2D_0A^m}{mn_0^m x_0^{m+2}}, \tag{11}$$

giving the solution

$$x_0(\tau) = \left[\frac{2(m+2)D_0A^m\tau}{mn_0^m}\right]^{1/(m+2)}, \tag{12}$$

Since $D(\mathfrak{n}) = D_0(\mathfrak{n}/n_0)^m$, non-linear diffusion is faster in dense regions than at lower concentrations, thus the *leading* front becomes the bottleneck of expansion. As a result, the solution is governed by the front motion, and this regime is different from regular diffusion, which propagates as the square root of time. Integrating this profile from $-x_0(\tau)$ to $x_0(\tau)$ we find $2N_0h(t) = bAh(t)$ ($2N_0$ is the initial total number of particles – or N_0 for each half-axis), which fixes the integration constant,

$$A = \frac{2N_0}{b}. \tag{13}$$

Here b is expressed through the beta-function,

$$b = B\left(\frac{1}{2}, \frac{1}{m} + 1\right) \tag{14}$$

Formulae (9), (12) and (13) define the intermediate asymptotics or similarity solution. This solution forms

a two-parameter family, with the first parameter being the initial total number of cells, $\mathfrak{N}(0) = 2N_0$, and the second parameter being an initial time, t_0, which enters through the integration limits in Eq. (10). Functions $\tau(t)$ and $h(t)$ are expressed through the growth rate term and for the simplest case of pure non-linear diffusion ($\gamma = 0$), one should set $h = 1$, $\tau = t$.

B. Diffusion lengths and parametrically driven similarity approximation

Consider the case of pure non-linear diffusion, $\gamma = 0$, $\tau = t$. As one can see from Eq. (9) the local diffusivity (which is proportional to $\mathfrak{n}^m$) has a parabolic profile inside the domain $-x_0 \le x \le x_0$,

$$D(x,t) = D_0 \left[\frac{2N_0}{x_0(t) b n_0}\right]^m \left[1 - \frac{x^2}{x_0^2(t)}\right]. \qquad (15)$$

It is instructive to compare the diffusion length, $L(x,t)$ associated with this diffusivity and the population size, x_0. Taking the maximal value of the diffusivity at $x = 0$ and using Eq. (12), we find

$$\frac{L(0,t)}{x_0(t)} = \frac{2^{1/2}}{x_0(t)} \left[\int_{t_0}^{t} D(0,t_1) dt_1\right]^{1/2} = \sqrt{\frac{m}{2}}\,. \qquad (16)$$

For strong non-linearity, $m \gg 1$, the diffusion length greatly exceeds the support of the distribution, $x_0(t)$. Correspondingly, the concentration profile inside the occupied domain, Eq. (9), is almost uniform. If the diffusion length exceeds the domain size many times over, under conditions of decreasing diffusivity, $D(0,t) \propto t^{-m/(m+2)}$, the equilibration of the similarity profile should be quick. To get a time scale perspective on this, let's compute the time t_x it takes for cells with diffusivity $D(0,t)$ to expand over the distance $x_0(t)$. Using Eq. (16), with integration ending at $L(0,t_x) = x_0(t)$, we obtain

$$\frac{t_x}{t} = \left(\frac{2}{m}\right)^{(m+2)/2}, \qquad (17)$$

which displays a super-exponential m-dependence, and implies that for large m the similarity solution, if perturbed, is quickly restored.

Close to the leading front, at any point inside, $|x| < x_0(t)$, $\Delta x = x_0 - |x| \ll x_0(t)$, the local diffusion length $L(x,t)$, although getting small, $L(x,t) \ll L(0,t)$, still greatly exceeds the distance to the front, $L(x,t) \gg \Delta x$. Indeed, the diffusivity there may be approximated by $D(x,t) \simeq 2D(0,t)(\Delta x/x_0)$, and the ratio of the diffusion length to the spatial scale is $L(x,t)/\Delta x \simeq m^{1/2}$. It exceeds the right-hand side of Eq. (16) by a factor of $\sqrt{2}$.

This has consequences for the stability of the similarity solution, Eq. (9). Such stability has been studied in [19] and later in [38]. Corrections to the leading order, $\mathfrak{n} \sim N_0/x_0(t) \propto t^{-1/(m+2)}$ were found to decay slowly, bounded by estimates $O[t^{-(3m+4)/(m+2)}]$ and $O[t^{(m+3)/(m+2)}]$, respectively, depending on the support of the initial condition [37]. In our case, with large m and compact support, the stability of the similarity solution significantly improves. Inside the main part of the concentration hull, where $\mathfrak{n}(0,t) - \mathfrak{n}(x,t) \ll \mathfrak{n}(0,t)$ and $D(0,t) - D(x,t) \ll D(0,t)$, the stability is bounded by the first eigenmode of the linear diffusion problem with diffusivity $\min_x \{D(x,t)\}$. This eigenmode has an exponential decay, $\exp(-cL^2/x_0^2) = e^{-cm}$, where c is some number, and we used Eq. (16). Close to the boundary, the same could be said about relaxation at small intervals, Δx. These estimates support the stability of the similarity solution and lead to a parametrically driven similarity approximation where the parameters are slowly affected by the inhomogeneous source/sink terms added to the non-linear diffusion equation.

Consider the implications of a large diffusion length (hence, short diffusion times), when the number of particles is slightly perturbed externally. When time makes a step dt, $\mathfrak{N}(t+dt)$ cells are mobile, and they occupy the domain $-x_0 \le x \le x_0$ which was prepared for them prior to this time step. For large non-linearity m, these cells diffuse around to become almost uniformly distributed with concentration $\mathfrak{N}(t+dt)/bx_0$. Note, that

$$\lim_{m\to\infty} b = \lim_{m\to\infty} B(\frac{1}{2}, \frac{1}{m} + 1) = 2. \qquad (18)$$

From the similarity solution viewpoint, the cells constituting $\mathfrak{N}(t+dt)$ are effectively plugged into a certain evolution time frame, where the elapsed time is adjusted to match a slightly modified similarity scenario. In this scenario, the same size $x_0(t)$ is achieved with the number of mobile cells $\mathfrak{N}(t+dt)$. As a result, the elapsed time t is adjusted by the value of a time offset, $t - t_{of}$. The width x_0 of the adjusted similarity solution can no longer be given by Eq. (12) (with $A \simeq \mathfrak{N}(t)/b$ from Eq. (13)), since $x_0(t)$ is dependent on the entire history of the time-dependent concentration $\mathfrak{N}(t)$ and offset t_{of}. One has to return to Eq. (11), which now reads

$$\frac{dx_0^{m+2}(t)}{dt} = \frac{2(m+2)D_0 \mathfrak{N}^m(t)}{m(bn_0)^m}. \qquad (19)$$

Note that this equation does not explicitly contain the time t, nor the time offset t_{of}. Therefore, the region of validity of Eq(19) should be larger: it should remain valid for a time-dependent total number of cells, as long as this number changes relatively slowly, in terms of diffusion times inside the hull.

To see this, let's compare the exact solution obtained in Sec. IV A with this approximation. Here cells are added not locally, with a growth rate γ, but globally, through the time-dependent total number of cells. This number, $\mathfrak{N}(t)$, changes more slowly than the relaxation time of the similarity solution t_x, Eq. (17). If we start from a pure non-linear diffusion problem which has $2N_0$ cells and no growth term, its domain size x_0 is given by

$$x_0(t) = \left[\frac{2(m+2)D_0 \mathfrak{N}(0)^m t}{m(bn_0)^m}\right]^{1/(m+2)}. \qquad (20)$$

Plugging here the total number of cells of the problem with the growth term included, i.e. substituting $\mathfrak{N} = 2N_0 h(t)$ for N_0, does not recover Eq. (12). Instead of $\tau(t)$, one incorrectly obtains $th^m(t)$. However, if the differential equation (19) is used, one finds

$$\begin{aligned} x_0^{m+2}(t) =& \frac{2^{m+1}(m+2)D_0 N_0^m}{m(bn_0)^m}\int_{t_0}^{t} h^m(t_1)dt_1 \\ =& \frac{2^{m+1}(m+2)D_0 N_0^m \tau(t)}{m(bn_0)^m}, \end{aligned} \tag{21}$$

which matches Eq. (12), after using Eq. (13). Here it is again assumed (c.f. Eq. (16)) that the lower limit of integration is such that the localized initial condition is forgotten.

To summarize, fast diffusion and slow hull expansion at $m \gg 1$ form the basis of what we call parametrically driven similarity approximation. It greatly simplifies the analysis, by reducing the study of a non-linear PDE for the concentration profile to solving an ODE for the location of the moving fronts. The essence of this approximation is to evolve the population through a set of similarity solutions, by properly adjusting the solution parameters in time. It is similar to other "adiabatic" invariants, such as adiabatic invariants in Hamiltonian systems [39].

C. Differential equations for both fronts

Still under the assumption of age-independent dynamics, we now add back the spatial diffusivity cutoff, Eq. ((6). This vanishing spatial diffusivity precludes cells at $\mathfrak{n} \geq n_0$ from participating in the front movement, and their subsequent evolution is irrelevant for the front region.

For a population wave advancing to the right on x-axis, the leading front moves with the speed dx_0/dt defined as the speed of the rightmost point, where $\mathfrak{n}(x_0, t) = 0$, while the trailing front moves with speed dx_1/dt, defined as the speed of the rightmost point where $\mathfrak{n}(x_1, t) = n_0$. Integrating Eq. (8) from x_1 to x_0, and using the formula

$$\begin{aligned} \frac{d\mathfrak{N}}{dt} =& \frac{d}{dt}\int_{x_1(t)}^{x_0(t)} \mathfrak{n}(x,t)\, dx \\ =& \int_{x_1(t)}^{x_0(t)} \frac{\partial \mathfrak{n}}{\partial t}\, dx + \mathfrak{n}(x_0,t)\frac{dx_0}{dt} - \mathfrak{n}(x_1,t)\, \frac{dx_1}{dt} \\ =& \int_{x_1(t)}^{x_0(t)} \frac{\partial \mathfrak{n}}{\partial t} dx - n_0\, \frac{dx_1}{dt}, \end{aligned} \tag{22}$$

we get

$$\mathfrak{N}' = \gamma(t)\mathfrak{N} - n_0 x_1'(t), \tag{23}$$

where prime denotes the time derivative d/dt. This equation is exact. Now, if changes in $x_1(t)$ are slow enough to preserve the applicability of the parametrically driven similarity solution, the propagation of the leading front is given by the approximation Eq. (19) with the following change: the point $x_1(t)$, where the diffusion flux vanishes, now plays the role of the point $x = 0$ of the previous section. Writing the left-hand side of Eq. (19) as $(m+2)x_0^{m+1}\, x_0'$ we should replace $x_0(t) \to x_0(t) - x_1(t)$ in the term x_0^{m+1}, but not in the term x_0'. Then,

$$(x_0 - x_1)^{m+1} x_0' = \frac{2D_0(2\mathfrak{N})^m}{m(n_0 b)^m}. \tag{24}$$

The normalization condition Eq. (13) is also applicable, in the form $x_0 - x_1 = 2\mathfrak{N}/n_0 b$. Equation (24) then becomes

$$x_0' = \frac{D_0 n_0 b}{m\mathfrak{N}}, \tag{25}$$

and therefore,

$$x_1' = \frac{D_0 n_0 b}{m\mathfrak{N}} - \frac{2\mathfrak{N}'}{n_0 b}. \tag{26}$$

Now, using Eq. (23), we get a closed equation for the total number of cells,

$$\frac{2-b}{b}\mathfrak{N}' = -\gamma(t)\mathfrak{N} + \frac{D_0 n_0^2 b}{m\mathfrak{N}}, \tag{27}$$

and multiplying by $\mathfrak{N}$,

$$\frac{2-b}{2b}(\mathfrak{N}^2)' + \gamma(t)\mathfrak{N}^2 = \frac{D_0 n_0^2 b}{m}, \tag{28}$$

one finds a closed linear mean-reverting ODE for $\mathfrak{N}^2(t)$, with solution

$$\mathfrak{N}^2(t) = N_0^2 e^{-\phi(t)} + \frac{2D_0 n_0^2 b^2}{m(2-b)}\int_{t_0}^{t} e^{\phi(t_1)-\phi(t)} dt_1, \tag{29}$$

$$\phi(t) = \frac{2b}{2-b}\int_{t_0}^{t} \gamma(\xi) d\xi. \tag{30}$$

For non-steady motion of the fronts, Eq. (28) for $\mathfrak{N}(t)$ may be substituted back into Eqs. (25), (26), with the wave width, $x_0 - x_1 = 2\mathfrak{N}/n_0 b$. As one can see, Eq. (27) inverts source and sink signs. The origin of this property may be traced to the number of cells needed to maintain sustainable growth given the growth rate, see also Eq. (35) below. Note that (i) additional sources *decrease* the number of cells in the wave, and vice versa, while (ii) an increase in the growth rate γ speeds up mean-reversion. These properties, if they are observed in population waves or swarms, could aid to model applications.

Derivation of Eq. (28) was based on the assumption that both fronts either move in the direction of the overall wave propagation, $x_0'(t) > 0$, or at least remain static, $x_1'(t) \geq 0$. The right-hand side of Eq. (25) is positive, and the leading front, $x_0(t)$, moves as assumed. However the right-hand side of Eq. (26) for the trailing front $x_1(t)$, may change sign. When this happens, the trailing front stops. The diffusivity is zero behind it, and therefore the

trailing front cannot go backward. Under these conditions Eq. (26) is no longer valid, and one has to revert to the exact equation Eq. (23) with $x_1' = 0$. To analyze this situation, one has to go back to the non-saturated case, $\mathfrak{n} < n_0$, and revisit the front motion along with the maximal concentration dynamics, $n_m(t) = \mathfrak{n}(0,t)$. Within our parametrically driven similarity approximation, the normalization condition reads in this case

$$2\mathfrak{N} = bn_m(x_0 - x_1). \tag{31}$$

This relation can be substituted into Eq. (24) for the leading front, which becomes,

$$x_0' = \frac{D_0 n_0 b}{m\mathfrak{N}} \left(\frac{n_m}{n_0}\right)^{m+1}. \tag{32}$$

We again find a closed system of ODEs for $x_0(t)$, $n_m(t)$ and $\mathfrak{N}(t)$, i.e. Eqs. (32), (31), and (23), where x_1 is constant. The latter is reduced to $\mathfrak{N}' = \gamma\mathfrak{N}$, since the trailing front is at rest.

It is straightforward to check our parametrically driven similarity approximation against exact similarity solutions in cases when the latter are available. This is discussed for the case of a steady-moving solution for a constant rate $\gamma(t) = \gamma_0$, and a "square-root-in-time" solution for a slowing wave with $\gamma_1 = \beta/t$; both cases are stable asymptotics, recovered by setting $\mathfrak{N}' = 0$, in Eq. (27).

1. *Wave traveling with constant speed*

For a constant growth rate $\gamma = \gamma_0 > 0$, supplied with a diffusivity cutoff, Eq. (8) has a steady traveling wave solution. One can make use of the substitution

$$\mathfrak{n}(x,t) = n_0\eta(z), \quad z = \frac{v(x-vt)}{D_0}, \tag{33}$$

where length is measured in units of D_0/v and time in units of D_0/v^2. Equation (8) then reads

$$\eta' + (f\eta')' + \kappa\eta = 0, \tag{34}$$

with the rescaled growth parameter $\kappa \equiv \gamma_0 D_0/v^2$, and $f(\eta)$ given in Eq. (6). Unlike Eq. (A7), Eq. (34) possesses translational invariance, as it should be for a steady-moving wave. The analytical solution of Eq. (34) is unavailable. We give details on the numerical solution in Appendix B. These numerical results can be compared with those obtained using the parametrically driven similarity approximation developed above. To establish steady motion of the fronts with speed v, we set $\mathfrak{N}' = 0$ in (28), and find

$$x_0 - x_1 = \frac{2\mathfrak{N}_0}{bn_0},\ v = v_0 \equiv \frac{\gamma_0\mathfrak{N}_0}{n_0},\ \mathfrak{N}_0^2 = \frac{D_0 b}{m\gamma_0} n_0^2. \tag{35}$$

The front moves with the speed given by the diffusion length over the time scale associated with the inverse growth rate. As the growth rate γ_0 increases, the speed of the population wave also increases as $\gamma_0^{1/2}$, while its width and the number of cells both decrease as $\gamma_0^{-1/2}$, thus keeping the concentration inside close to n_0 and independent o γ_0.

Let us compare the concentration profile of the similarity solution and Eq. (34). One can see that sufficiently close to the fronts the exact solution is well described by the similarity approximation Eq. (35), for any m. Indeed, with the dimensionless units of this subsection, the length of the half-hull is (to leading order, m^{-1}) $vx_0/D_0 = 2/m$, and Eq. (9) reads

$$\eta(x') = \left(1 - \frac{m^2 x'^2}{4}\right)^{1/m}, \quad x \le \frac{2}{m}, \quad \kappa_0 = \frac{m}{b}. \tag{36}$$

In the vicinity of the leading front $\varepsilon = 2/m - x' \ll 1$ we have

$$\eta = (m\varepsilon)^{1/m}. \tag{37}$$

This asymptotic form satisfies Eq. (34) near the leading front, $\eta' = (\eta^m\eta')'$ with $\eta(0) = 0$, where the slopes are high, and the source term is irrelevant. On the trailing front, the concentration profile is almost flat, and (36) reduces to $\eta = 1 - mx'^2/4$, $x' \ll 1$. This asymptotic form satisfies $0 = \kappa\eta + (\eta^m\eta')'$, i.e. Eq. (34) without the velocity term. If $m \gg 1$, an additional study shows that the approximate profile Eq. (36) is close to the solution of Eq. (34) everywhere between the fronts, including the region where all three terms are of the same order. Figures 2 and 3 below compare numerical values for the speed, front width, and concentration profile with analytical formulae obtained by means of the parametrically driven similarity approximation.

2. *Slowing wave*

In this example, we consider time-dependent growth rates of the type, $\gamma(t) = \beta/t$, $\beta > 0$. With unrestricted diffusion, the population follows a power-law, $\mathfrak{N}(t) = 2N_0(t/t_0)^\beta$, and so does the population size, $x_0 \propto t/t_0)^{(m\beta+1)/(m+2)}$ (for details see Appendix C). It can be shown that the diffusivity cutoff matters for $\beta > 1/2$, and leads to a slowing-down population wave, generating a cutoff concentration n_0 behind the trailing front. This motivates the use of $\mathfrak{n}(x,t) = n_0 g(z)$. Lengths are measured in units of L, and times in units of c^2L^2/D_0, where c is an adjustable dimensionless coefficient. For Eq. (8) we introduce a similarity variable,

$$z = \frac{1}{x_0(t)}\left[x + \int v(t)dt\right], \tag{38}$$

(the constant of integration is disregarded here, as the similarity solution is valid when the initial condition is forgotten) and obtain

$$g'\left(-z\frac{x_0'}{x_0} + \frac{v}{x_0}\right) = \frac{c^2}{x_0^2}(fg')' + \frac{\beta}{t}g. \tag{39}$$

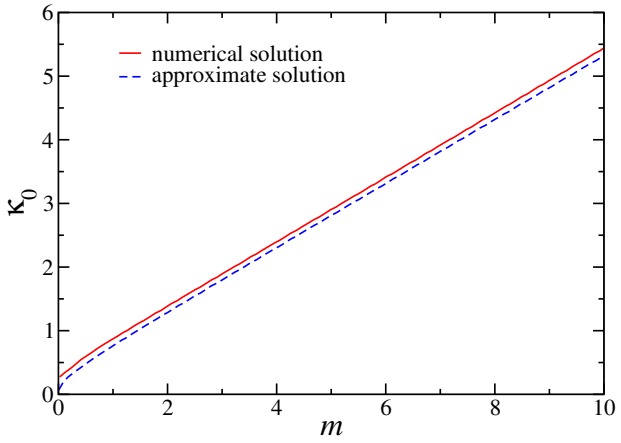

(a)

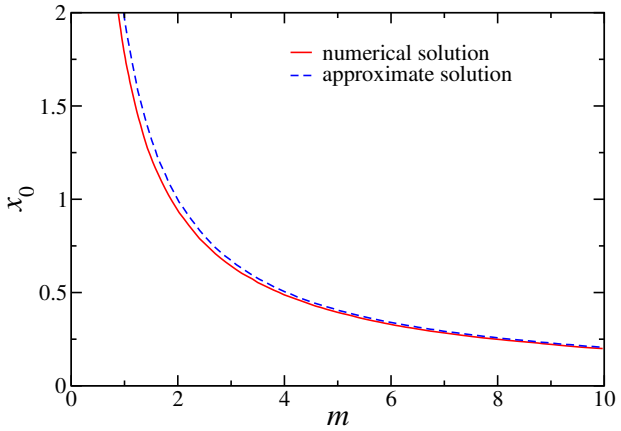

(b)

FIG. 2. Comparison of the dimensionless velocity selection $\kappa_0(m)$ (a), and the dimensionless front width $x_0(m)$ (b) for a steady-moving front, obtained by numerical integration of Eq. (34) (red solid curve), and the similarity approximations (blue dashed curve) given respectively by $\kappa_0 = m[B(\frac{1}{2}, \frac{1}{m} + 1)]^{-1}$ and $x_0 = 2/m$. Asymptotic analysis and numerical analysis both show that the leading asymptotic behavior of the entire solution of (34) is the same as (9) at large m, and represents a good approximation even at $m \sim 1$.

For consistency, one should set $x_0 = ct^{1/2}$, $v = ux_0/2t$, and we obtain

$$(fg')' + \frac{z-u}{2}g' + \beta g = 0. \qquad (40)$$

The analytical solution of this ODE is unavailable.

Using the parametrically driven similarity approximation, one substitutes $\gamma(t) = \beta/t$ into Eq. (29), and obtains after integration (by retaining only the leading time-dependence),

$$\mathfrak{N}(t) = n_0 b \left[\frac{2D_0 t}{m}(2b\beta - b + 2)\right]^{1/2}. \qquad (41)$$

The leading front moves according to Eq. (25), which

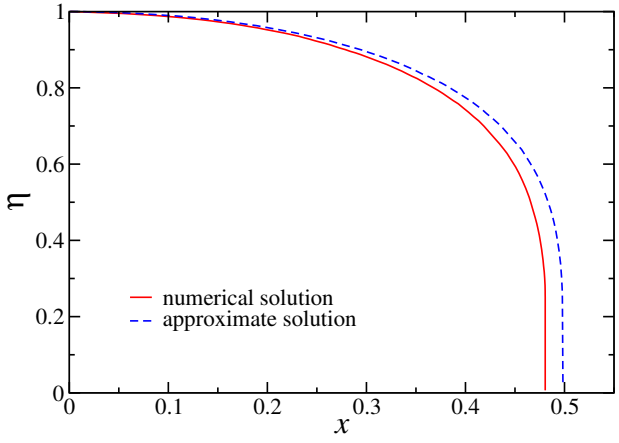

FIG. 3. Comparison of the solution $\eta(x)$ of (34) (solid red curve) and the approximate solution (36) (blue dashed curve),T for a steady-moving front. The difference between solutions vanishes with $m \to \infty$. In this figure, $m = 4$. The rightmost points are $x_0 = 0.482573$ for the numerical solution, and $x_0 = 2/m = 0.5$ for the approximate solution, c.f. Fig. 2(b).

may be combined with Eq. (41) to give

$$x_0(t) = \left[\frac{2D_0 t}{m}(2b\beta - b + 2)\right]^{1/2}. \qquad (42)$$

Within the same approximation, Fig. 4 shows that the numerically selected value of the reduced speed u is well approximated by $u \approx (2/m)^{1/2}(2b\beta - b + 2)^{1/2}$.

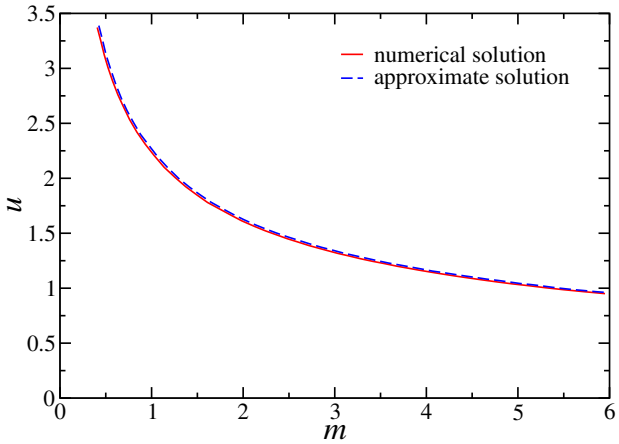

FIG. 4. Comparison of the selected parameter u based on the numerical solution of Eq. (40) (red solid curve) and the approximate solution Eq. (42) (blue dashed curve), for a slowing wave with $\beta = 0.7$. One can barely see the gap between the two curves in the upper-left corner, where $m < 1$.

D. Age-structured waves

We now apply the parameter-driven similarity solution method to the full model, with constant growth rate, $\gamma_0 > 0$. Integrating Eq. (5) over the x-axis between the trailing and leading fronts, and introducing the age-density, $N(\theta,t) = \int n(x,\theta,t)dx$, we get an age-resolved analog of Eq. (23),

$$\frac{\partial N}{\partial t} + \frac{\partial N}{\partial \theta} = a\frac{\partial^2 N}{\partial \theta^2} + \gamma_0 N - n(x_1,\theta,t)\frac{dx_1}{dt}. \tag{43}$$

This equation is exact, and valid for both mobile and immobile cells, c.f. Eq. (23). Due to the last term, this equation is not closed. In this subsection we further restrict ourselves to the case when both leading and trailing fronts are in motion,

In the similarity solution for mobile cells, the density $n(x,\theta,t)$ reaches its maximum at the trailing front, $n(x_1,\theta,t) = n_m(\theta,t)$. The maximal age-density satisfies the same relationship as we have seen in Eq. (31),

$$2N(\theta,t) = bn_m(\theta,t)(x_0 - x_1), \tag{44}$$

with b given by Eq. (14). Therefore,

$$\frac{\partial N}{\partial t} + \frac{\partial N}{\partial \theta} = a\frac{\partial^2 N}{\partial \theta^2} + \gamma_0 N - \frac{2N}{b(x_0-x_1)}\frac{dx_1}{dt}. \tag{45}$$

If diffusivity is at its maximum, $D = D_0$, and both fronts advance, the total number of mobile cells is simply,

$$\begin{aligned} 2\mathfrak{N}(t) &= 2\int_{\theta_0}^{\theta_e} N(\theta,t)d\theta = b(x_0-x_1)\int_{\theta_0}^{\theta_e} n_m(\theta,t)d\theta \\ &= n_0 b(x_0 - x_1), \end{aligned} \tag{46}$$

and, similar to Eq. (25),

$$x_0' = \frac{D_0 n_0 b}{m\mathfrak{N}(t)} = \frac{\gamma_0 \mathfrak{N}_0^2}{n_0 \mathfrak{N}(t)}. \tag{47}$$

Using Eq. (46) and its time-derivative, along with Eq. (47) in Eq. (45), the following closure results,

$$\begin{aligned} &\frac{\partial N}{\partial t} + \frac{\partial N}{\partial \theta} = a\frac{\partial^2 N}{\partial \theta^2} + \tilde{\gamma} N, \\ &\tilde{\gamma} = \gamma_0 + \frac{2}{b\mathfrak{N}}\frac{d\mathfrak{N}}{dt} - \frac{\gamma_0 \mathfrak{N}_0^2}{\mathfrak{N}^2}, \end{aligned} \tag{48}$$

where we used (35). The steady-moving wave of Sec. IV C 1 is recovered by setting both $\tilde{\gamma}$ and $d\mathfrak{N}/dt$ to zero.

Integrating Eq. (48) over mobile ages and simplifying, one finds

$$\frac{\partial \mathfrak{N}}{\partial t} = \frac{b}{2-b}\left(F + \gamma_0 \mathfrak{N} - \frac{\gamma_0 \mathfrak{N}_0^2}{\mathfrak{N}}\right), \tag{49}$$

with non-local sources/sinks,

$$F = -N(\theta_e) + N(\theta_0) + a\left(\frac{\partial N}{\partial \theta}\right)\Big|_{\theta_0}^{\theta_e}. \tag{50}$$

Since $b < 2$, see Eq. (14), this equation is mean-reverting. Equation (49) was derived for large $m \gg 1$ where $2-b \ll 1$, see Eq. (18), and, to the leading order, one can set its right-hand side to zero, to find the "equilibrium" total number of mobile cells in the wave,

$$\mathfrak{N} = \sqrt{\mathfrak{N}_0^2 + \frac{F^2}{4\gamma_0^2}} - \frac{F}{2\gamma_0}. \tag{51}$$

If the mobile population only has ages within the interval $\theta_0 < \theta < \theta_e$, or has an age-independent density, then $F = 0$, and (51) reduces to (35). The slope of the steepest part of the supercycles trajectories, in Figs. 9, 10 below, was indeed found to be the speed of the age-uniform wave, v_0 (Eq. (35)).

Consider now a steady-moving age-structured wave, where the mobile population is not small only in the vicinity of the terminal age, $\theta = \theta_e$, so that $F = -N(\theta_e) + aN_\theta(\theta_e)$ in (50). We expect the most populous age-group to be there, given the life cycle in presence of Malthusian growth. For a steady-moving wave, Eq. (48) reads,

$$aN'' - N' + \tilde{\gamma} N = 0. \tag{52}$$

We are after a solution, $N = C\exp[\lambda(\theta - \theta_e)]$, with integration constant C, and positive eigenvalue λ. Then, $N(\theta_e) = C$, $N_\theta(\theta_e) = \lambda C$, and the total number of mobile cells is $\mathfrak{N} = C/\lambda$. Equations (51) and (52) give

$$a\lambda^2 - \lambda + \gamma_0\left(1 - \frac{\mathfrak{N}_0^2\lambda^2}{C^2}\right) = 0, \tag{53}$$

with two unknowns, C and λ. It means that there is a family of such mobile solutions, and the velocity selection occurs via interaction with the immobile cells.

The immobile cells also obey Eq. (43). Between the fronts of the steady-moving wave, $x_1 \le x \le x_0$, the density of immobile cells, $n(x,\theta)$, is independent of x in our approximation, and therefore $N(\theta) = n(\theta)(x_0 - x_1 - \theta x_0')$. The density $N(\theta)$ then has a minimum at $\theta = \theta_0$. Once a small amount of cells becomes mobile at $\theta = \theta_0$ their concentration grows exponentially as per the solution of Eq. (52) above. To the leading order we should set $x_0 - x_1 = x_0'\theta_0$. Together with Eqs. (46) and (47) this determines the number of cells in the wave and the velocity of the age-structured wave,

$$\mathfrak{N} = b\, n_0 \left(\frac{D_0\theta_0}{2m}\right)^{1/2}, \quad v_s = \left(\frac{2D_0}{m\,\theta_0}\right)^{1/2}. \tag{54}$$

The speed v_s does not depend on the Malthusian growth parameter, unlike the speed of the age-uniform wave,

$v_0 \propto \gamma_0^{1/2}$ in (35). The eigenvalues,

$$\lambda_{1,2} = \frac{1}{2a}\left[1 \pm \sqrt{1 - 4a\left(\gamma_0 - \frac{2}{b\theta_0}\right)}\right], \qquad (55)$$

are both real and positive, provided that

$$\gamma_0 \le \gamma_1(a) = \frac{8a + b\,\theta_0}{4a\,b\,\theta_0}. \qquad (56)$$

For small $a \ll b\,\theta_0/8$ this gives a condition $4a\gamma_0 < 1$, which can be traced to the Green function of non-interacting cells. Indeed, expanding the exponent in Eq. (58) below, one finds a term, $(\gamma_0 - 1/4a)t$, controlling population buildup at a fixed age, and also pointing to the parameter combination $a\gamma_0$. While the condition of no population buildup at a given age is natural for cells of a single organism, there is no reason why it should hold true for less organized communities, such as swarms.

The derivation above also relies on sufficiently large γ_0, namely, $\exp[\lambda(\theta_e - \theta_0)] \gg 1$, which for small a reduces to $\exp[(\gamma_0 - 2/b\theta_0)(\theta_e - \theta_0)] \gg 1$. When this condition does not hold at $\gamma \lesssim 2/b\theta_0$, neighboring generations mix in the wave, and although the age distribution $N(\theta, t)$ still has a minimum near $\theta = \theta_0$, this minimum is shallow, and linear growth dominates.

At $\gamma_0 \gtrsim \gamma_1$ the model also exhibits linear growth, achieved by a balance between aging and strong Malthusian growth, accompanied by diffusion down the age-axis. These conditions bound a region where the supercycles dominate, see Sec. V B and Fig. 11 below.

E. The mobility threshold

Next we will examine in more detail the evolution of the moving fronts in the parametrically driven similarity approximation, as compared with the full solution of the model PDE Eq. (5). We will also consider how the age distribution reshapes when spatial diffusion sets in at the mobility threshold, θ_0, and when cells reach the age θ_e, and lose mobility.

In presence of small age diffusion with the source $N_0\delta(\theta)\delta(t)$, where δ is the Dirac delta function, the evolution along the age axis is initially independent of spatial transport. An age-localized initial condition in a spatially uniform case evolves as described by the spatially-integrated equation Eq. (5), resulting in

$$\frac{\partial N}{\partial t} + \frac{\partial N}{\partial \theta} = a\frac{\partial^2 N}{\partial \theta^2} + \gamma_0 N + N_0\delta(t)\delta(\theta). \qquad (57)$$

with solution given by the Green function,

$$N(\theta, t) = N_0 G(\theta, t) = \frac{N_0}{(4\pi a t)^{1/2}} \exp\left[\gamma_0 t - \frac{(\theta - t)^2}{4at}\right]. \qquad (58)$$

When mobile cells first appear, their total number is given by

$$\mathfrak{N}(t) = \frac{N_0}{(4\pi a t)^{1/2}} \int_{\theta_0}^{\infty} \exp\left[\gamma_0 t - \frac{(\theta - t)^2}{4at}\right] d\theta$$
$$= N_0 e^{\gamma_0 t} c\left(\frac{\theta_0 - t}{\sqrt{4at}}\right), \quad c(\xi) = \frac{1}{2}\mathrm{erfc}(\xi), \qquad (59)$$

and the leading front begins to move according to Eq. (47) with $x_1 = 0$. The leading front position is

$$x_0^{m+2}(t) = \frac{2^{m+1}(m+2)D_0 N_0^m T_1(t)}{m(bn_0)^m},$$
$$T_1(t) = \int_0^t e^{m\gamma_0\xi}\; c^{\,m}\left(\frac{\theta_0 - \xi}{\sqrt{4a\xi}}\right) d\xi. \qquad (60)$$

If $a = 0$ we recover $T_1(t) = \tau(t) = \{\exp[m\gamma_0(t - \theta_0)] - 1\}/m\gamma_0$, at $t > \theta_0$.

Let us again denote as t_1 the moment when the maximal concentration inside the front reaches $\mathfrak{n} = n_0$. It satisfies the equation $2\mathfrak{N}(t_1) = bx_0(t_1)$. The time t_1 depends on the initial concentration N_0, and could be larger or smaller than θ_0. Suppose a traveling wave solution is eventually established. From the moment t_1 onward, the trailing front x_1 moves over the interval where cells were initially located. While this happens, Eq. (59) is no longer valid and instead the total number of cells is governed by

$$\mathfrak{N}' = \gamma_0\mathfrak{N} - n_0 x_1' + \frac{w_0 - x_1}{w_0}\; N_0 G(\theta_0, t), \qquad (61)$$

where w_0 is the span of the initial condition along the x-axis. Using Eq. (25) and $x_0 - x_1 = 2\mathfrak{N}/n_0 b$, we get a closed system of two first-order ODEs and a linear equation. This system can be solved numerically, see Figs. 5, 6. These figures also contain a comparison with the full PDE numerical solution.

We now describe what happens with the age distribution at the mobility threshold. Once the trailing front is in motion the age-distribution begins to change. An age group of width $d\theta$ which crosses the mobility threshold at time t makes a contribution to the total number of cells which is equal to $d\theta N_0 G(\theta_0, t)\max[0, 1 - x_1(t)/w_0]$. The part of the age distribution where ages do not exceed θ_0 by the time t_2, where $x_1(t_2) = w_0$, does not participate in subsequent motion and it is left behind the trailing front. Adjacent parts of the distribution, where ages do not exceed θ_0 by the time when the trailing front starts moving, are diminished in proportion to $[1 - x_1(t)/w_0]$. The maximum of the age distribution advances in age, by a certain positive amount $\Delta\theta_0 \sim (a\theta_0)^{1/2}\log(\theta_0/a)$, and its standard deviation is diminished, see Fig. 7. The reason the standard deviation is more resilient to the threshold is that, when the trailing front $x_1(t)$ approaches the right end of the initial condition w_0, the wave is not sufficiently populated by the cells coming from the initial condition, and the wave has to wait until the growth term makes its

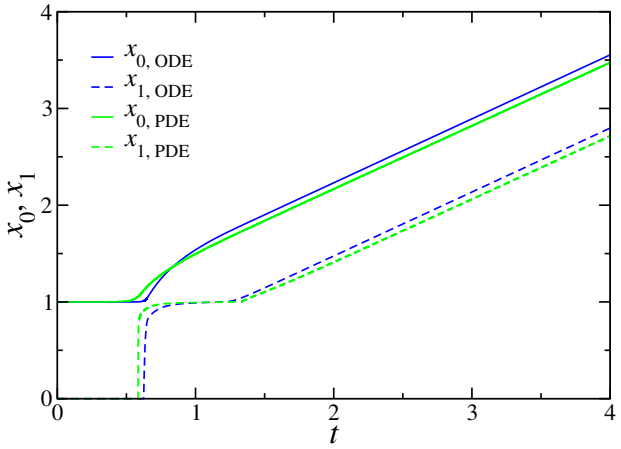

FIG. 5. Behavior of the leading and trailing fronts when the distribution becomes mobile at $\theta = \theta_0$. For nonzero age diffusivity a, cells do not acquire mobility synchronously, even though they were initially synchronized at age $\theta = 0$ through the initial condition. As a consequence, the fronts set into motion at times $t < \theta_0$. One can observe that the trailing front, once it starts moving, quickly reaches an intermediate steady state and awaits for accumulation of cells due to growth to continue advancing. At larger times a steady-moving wave is formed. Parameters: $m = 4$, $\theta_0 = 1$, $D_0 = 1$, $g_0 = 1$, $a = 0.05$, $w_0 = 1$, $n_0 = 1$, $N_0 = 10$. Blue lines are solutions of the system of ODEs for x_0, x_1, $\mathfrak{N}$, n_m from Sec. IV D, green lines are numerical solutions of the full model PDE (5).

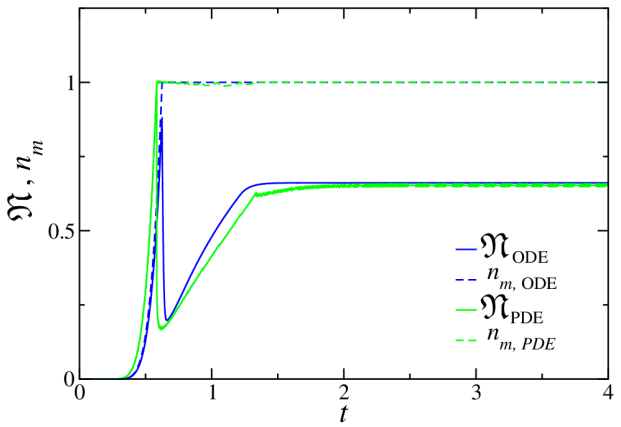

FIG. 6. Time dependence of the total number of mobile cells, $\mathfrak{N}(t)$ (solid line) and maximal concentration $n_m = \mathfrak{n}(x_1(t), t)$ (dot-dashed line). Parameters are the same as in Fig. 5. When the trailing front starts moving the maximal concentration remains equal to the cutoff value $n_0 = 1$. The front first shrinks, and the total number of cells takes a dip. Then there is recovery and the trailing front finally clears the initial condition support w_0. By then the steady-moving wave is fully formed. Blue lines are the solutions of the ODEs for x_0, x_1, $\mathfrak{N}$, n_m from Sec. IV D, green lines are numerical solutions of the full model PDE (5).

contribution. At small a and large total number of initial cells N_0, upon passing the mobility threshold, only a fraction of the initial age-distribution remains in the

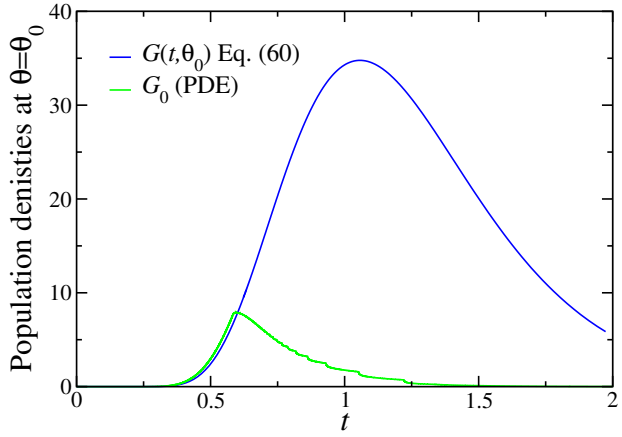

FIG. 7. Reshaping of the age distribution at the mobility threshold, $\theta = \theta_0$. Parameters are the same as in Fig. 5. At times $t \simeq 0.6$ when the trailing front x_1 begins to move (see Fig. 5), the population at the threshold, $G_0 = n(t, \theta_0, x_1)$ is reshaped. The blue line is the distribution G given by Eq. (58) at $\theta = \theta_0$, and represents the "incoming" distribution, observed at $\theta = \theta_0$ with $D_0 = 0$, when the spatial wave does not move, and does not cut off the tail of this age distribution. The green line is obtained by numerically solving Eq. (5).

moving front.

As can be seen in Fig. 7, the age-advanced cells are selected by the mobility threshold. At the mobility threshold, an initially age-synchronized population has an age width of $\sigma_0 = (2a\theta_0)^{1/2}$, and this time scale could be smaller or larger than γ_0^{-1} notwithstanding the restriction $4a\gamma_0 \lesssim 1$. If $a\theta_0\gamma_0^2 \ll 1$, then age diffusivity plays a small role, and all ages are retained in the wave. Therefore the width of the age distribution is almost unchanged while crossing the threshold, at least during the first cycle. In the opposite case, $a\theta_0\gamma_0^2 \gg 1$, the age distribution after the threshold narrows down to γ_0^{-1}.

As cells age and reach the terminal age, θ_e, the wave also loses particles, this time due to rebirth. During this process the cells which experienced rebirth earlier, and cease moving, are passed over by age-delayed cells. The age distribution of the residual population narrows. Both thresholds act as distribution sharpeners, with the mobility threshold θ_0 decreasing and terminal age θ_e increasing the supercycle period. In turn, the dispersion of age distribution allows the mobile phase to occupy a time window exceeding $\theta_e - \theta_0$, thus aiding to spatial growth.

V. PROPERTIES OF SUPERCYCLES

This section discusses developed supercycles. Consider first the case without age diffusion, $a = 0$, where any nonuniform age structure will display age periodicity with period θ_e. Suppose the initial population, $N_0\delta(\theta)\delta(t)$, is created in the interval $0 \le x \le w_0$ (c.f. previous section). In Fig. 8, the arrow (a) points at an initial state

with $w_0 = 1$. For times $t < \theta_0$ cells only grow, and their number reaches $N_0 e^{\gamma_0 \theta_0}$ when they acquire mobility at $\theta_0 = 1$ in (b). As we only have one age group, we can simplify concentration-related transient behavior, and choose the initial population parameters N_0 to satisfy condition Eq. (46), $2N_0 e^{\gamma_0 \theta_0} = n_0 b x_0(0)$. Then all the criteria of a steady-moving wave considered in IV C 1 are met, and a traveling wave forms.

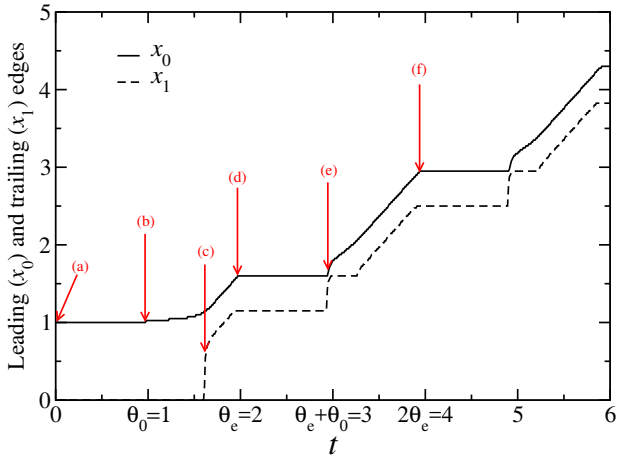

FIG. 8. Simulation at $a = 0$, $\theta_e = 2$, $\theta_0 = 1$, $\gamma_0 = 4$, $m = 4$ and initial population $N_0\delta(\theta)$. See text for the description of population stages (a–f).

If the width of the steady-moving front, w_0, is larger than the initial size, $x_0(0)$, the leading front will initially move either by itself, or with the trailing front advancing more slowly than the leading front, until the growing front width reaches its steady-state value. In the opposite case, the trailing front will advance with a jump (c), to reach the steady state. Upon reaching the maximal age at $t = \theta_e = 2$ in (d) (also in (f)), the entire wave stops, and the next cycle begins. For sufficiently large m, when the concentration profile is almost uniform inside the front, only the immediate vicinity of the leading front will be mobile in the next expansion phase, at $t = \theta_e + \theta_0$ (e). This expansion will take place in a region of smaller width, w_1, where the concentration Eq. (9) satisfies $\mathfrak{n}(x, \theta_e + \theta_0) \le n_0$. The mobile concentration profile is steeper than the steady-moving shape, and there will be a transient period when cells reshape the profile via diffusion. The concentration at the trailing front n_m falls below the diffusivity cutoff, n_0, so that the trailing front will be initially at rest. When the mobility edge is passed, the similarity profile, associated with the remaining cells is quickly achieved, and the front will continue expansion with a time-dependent width until the terminal age $2\theta_e$. If, in addition, the parameter $e^{\gamma_0(\theta_e - \theta_0)}$ is large enough, the steady-moving wave is established.

Small nonzero age diffusivity introduces lifecycle variability with the effect that the period of the population cycles shortens with respect to the life cycle of individual cells (Fig. 9). The population expansion phases fade out as a increases, until age mixing is sufficiently strong so that cycles disappear. The effect of the Malthusian

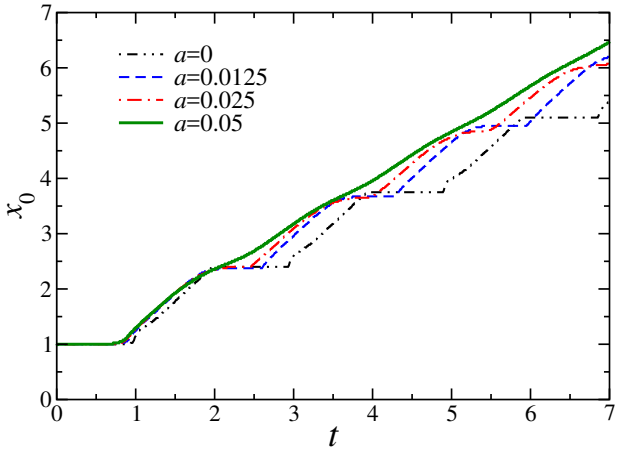

FIG. 9. Leading fronts for different values of the age diffusivity a, with the parameters $\theta_e = 2$, $\theta_0 = 1$, $\gamma_0 = 4$, $m = 4$ and peaked initial population $N_0\delta(\theta)$.

growth parameter is different. For a given age diffusivity a, which in any case is restricted to values $a \ll \theta_0$, there exists an interval of γ_0 for which supercycles may exist. This is shown in Fig. 10. Steady cycles develop for this set of parameters between $\gamma_0 \approx 3$, and $\gamma_0 \approx 15$.

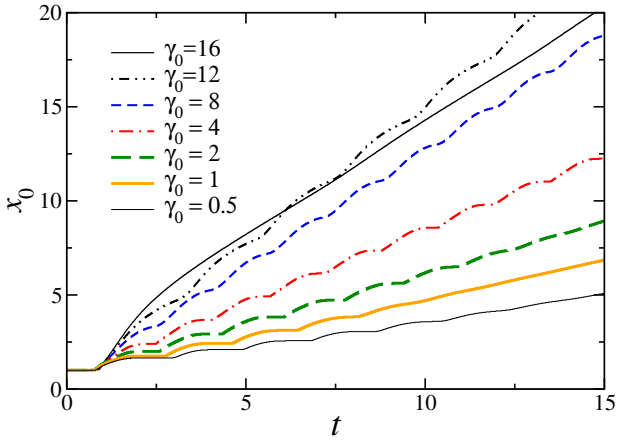

FIG. 10. Leading fronts for different values of the Malthusian growth parameter γ_0, with $\theta_e = 2$, $\theta_0 = 1$, $a = 0.02$, $m = 4$ and peaked initial population $N_0\delta(\theta)$.

The (a, γ_0) parameter region which supports supercycles is further discussed in Sec. V B.

A. Relaxation of bimodal age distributions

When cell ages do not coincide, there is a mechanism which offers competitive advantage to cell groups of close ages. Consider two coexisting age groups, A and B, created by the initial condition. Suppose also, that the

group B, reaches the mobility edge, θ_0, first, triggering spatial expansion of B alone. If conditions are right, i.e the growth rate and age difference are large enough, the wave may leave A entirely behind the trailing front. The mobility edge contributes to age segregation, benefiting age-advanced groups, and shortens supercycle period, if applicable.

At the terminal age, θ_e, this behavior could be inverted. If A and B are both found inside a traveling wave, age-advanced B stops first upon reaching θ_e, and A spreads alone, possibly leaving group B behind. Selective mobility termination favors age-delayed groups and age segregation. It lengthens the supercycle period.

We further note that in this system, an exponential growth is followed by shrinkage of the future mobile population down to the immediate vicinity of the leading front. Repetitive application of two such competing procedures could lead to complex intermediate behavior. Both mobility changes contribute to narrowing the age structure, counteracting age diffusion, eliminating outliers, and promoting cells from the tails of age distribution.

B. The period, T, and average front speed, $\bar{v}$, of supercycles

We now discuss selected properties of supercycles and linear growth, and the dependence of these properties on two model parameters, a, γ_0. The supercycle domain introduced in Sec. IV D is shown in Fig. 11 using axes (a, γ_0^{-1}).

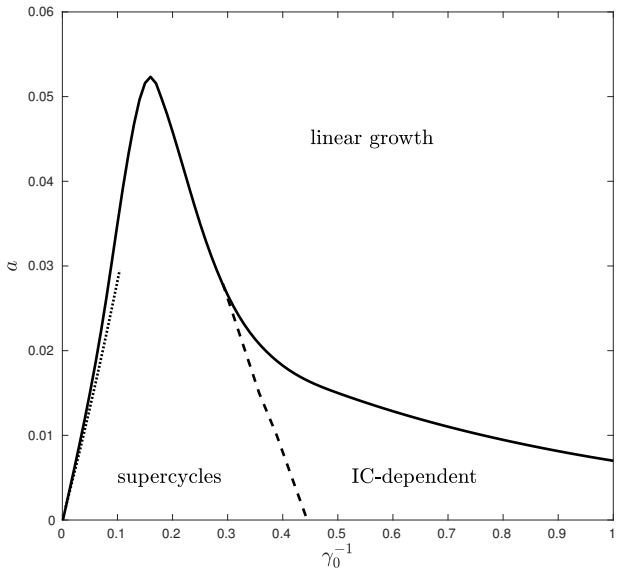

FIG. 11. Numerically obtained "phase diagram" of the types of long-term asymptotic solutions. 'IC-dependent' labels the domain where both linear growth and cyclic attractors coexist, see text. Parameters: $\theta_0 = 1$, $\theta_e = 2$, $m = 4$, $D_0 = 1$. The dotted line passing through the origin is given by Eq. (56).

In the domain labeled 'IC-dependent', supercycles form only for sufficiently peaked initial conditions, and then tend to spend relatively long times in the consolidation phases. For a peaked initial condition, the leading front and trailing front both stop during the immobile (consolidation) phase.

In the domain 'supercycles', even for age-uniform initial conditions, cycles become the long-term asymptotic. Close to the dashed boundary their amplitude vanishes for age-uniform initial conditions.

Inside a sub-domain with $a\gamma_0 \lesssim 0.1$ both fronts stop completely during consolidation phases, and consecutive generations do not mix much during the expansion phase. As γ_0 grows for a fixed a, first the effect of the mobility edge dominates, and the period T becomes shorter than θ_e (see Fig. 10). While the cycle-averaged front speed $\bar{v}$ is, of course, lesser than v_0 given by Eq. (35), $\bar{v}$ may exceed the fraction $1-\theta_0/\theta_e$ of v_0, which is the fraction of life cycle any given cell can be mobile in the model. This is a beneficial property of supercycles: due to incomplete synchronization along the age-axis, the collective wave is able to move for a larger fraction of elapsed time than any participating cell.

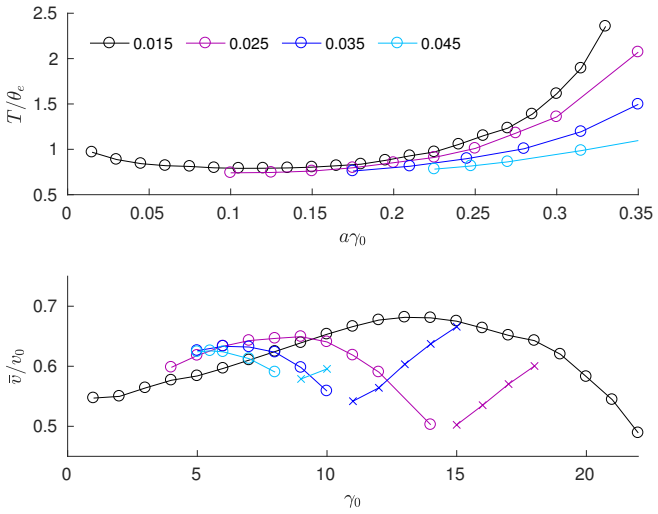

FIG. 12. Top: Dependence of the scaled supercycle period, T/θ_e, on the parameter product $a\gamma_0$. Here, $0.015 \le a \le 0.045$ (values and color coding shown in the legend), $1 \le \gamma_0 \le 21$. Bottom figure: dependence of the cycle-averaged speed, $\bar{v}/v_0$, on the growth rate, γ_0, with v_0 given by Eq. (35). $\circ$-markers show front speeds while supercycling, and $\times$-markers show front speeds with linear growth. The color coding is the same, and the other parameters are given in the caption of Fig. 11. See text for more details.

In the remaining part of the 'supercycles' domain in Fig.11, the leading front and then the trailing front no longer stop for consolidation as γ_0 grows. At small a, the period $T(a, \gamma_0)$ reaches a *minimum* and then increases, see top Fig. 12. For larger a, the period does not have a minimum: it increases with γ_0 once supercycles appear, as shown by the blue colored lines in the same figure. In this region of the parameter domain, the distribution

near the terminal age acquires more and more significance with γ_0, and the cycle period can significantly exceed θ_e. Notably, the front speed, $\bar{v}$ reaches a local *maximum* with γ_0 in the supercycling regime as a function of γ_0. The growth rate, γ_0, of the speed maximum is larger than the growth rate corresponding to the minimum of the cycle period, if the latter exists. Past the speed maximum, as the growth rate γ_0 further increases, the wave speed reaches a local *minimum*, in units of v_0. Past that point, the front speed resumes its increase with γ_0, see $\times$-markers.

At low a, at the border of 'supercycles' and further inside the 'IC-dependent' domain in Fig. 11, we observed prolonged transients and more complex supercycles.

VI. OBSERVATIONS OF SUPERCYCLIC BEHAVIOR

While discussing possible applications, there is a risk of nominating any adaptable internal oscillator as the driver of cyclic behavior, or delegating the driving to a relevant external (and very complex, such as climatic) variable. Given that the number of possible explanatory combinations is large, the search might simply terminate at the first statistical success. Below we discuss three selected examples where cyclical behavior is observed, the time scales can not be related to any known driver with certainty, and even if we find a driver operating at the observed time scales, it is unclear why it should lead to cycles. We hope that the present model will encourage quantitative studies in these systems.

A. Intra-annual thallus growth of lychen *Parmelia conspersa*

Cyclic growth is *sometimes* observed in the growth of thallus lobes of lichens on intra-annual time scales, see Fig. 2 in [3]. We replot these data here as a cumulative curve, displaying steps, to facilitate comparison with the model. The shape of the steps in Fig. 13 is similar to the leading front profiles among the curves of Fig. 1, and we borrow the parameter value $m = 4$ for the estimate below. By regressing the logarithm of the entire colony area (not only terminal lobes) on time, one finds $1/\gamma_0 \sim 20 \pm 2$ months. The typical top front speeds observed in the experiment were $v = 0.8$ mm/mon, so that

$$D_0 = \frac{mv^2}{2\gamma_0} \sim 25 \frac{\text{mm}^2}{\text{mon}} \tag{62}$$

Not much is known about the age diffusion in lichen lobes, but it cannot exceed $a \simeq 1$ mon (see below). The product $a\gamma_0 \lesssim 0.05$ is then likely to be small, and the cycle period should be close to θ_e, see Fig. 12. In the experiment, it was observed that the period, $T \simeq 3.8$ mon, and dormant or consolidation phases (widths of steps in Fig. 13) are close to $\theta_0 \simeq 1$ months. R.A. Armstrong and coauthors, who have studied *Parmelia conspersa*, identified the "internal driver" as follows: "The data suggest the hypothesis that lobes of *P. conspersa* exhibit a pattern of cyclic radial growth determined, in part, by lobe division" [3].

While the overall shapes of many foliose thalli are somewhat reminiscent of gradient-controlled Hele-Shaw flows, such flows, *per se* do not require or prescribe any periodicity. We note that lichens are symbiotic communities, and one should consider mechanisms where one of the bionts has to accumulate enough resources before continuing its growth. In the case of *P. conspersa* the timescale of T above is unlikely to be associated with the photobiont, as its reproduction is fully controlled or arrested by the mycobiont depending on location within the lichen [40]. It all then points to the mycobiont life cycle. While we are unaware of the dedicated life cycle studies of *P. conspersa* mycobiont(s), these life cycles in other lichen do last months, [41, 42]. The arrested development inside the lichen colony (similar to suppressed mobility inside bacterial colony of *P. mirabilis*, [17]) motivated us to disregard the region behind the trailing front in the model.

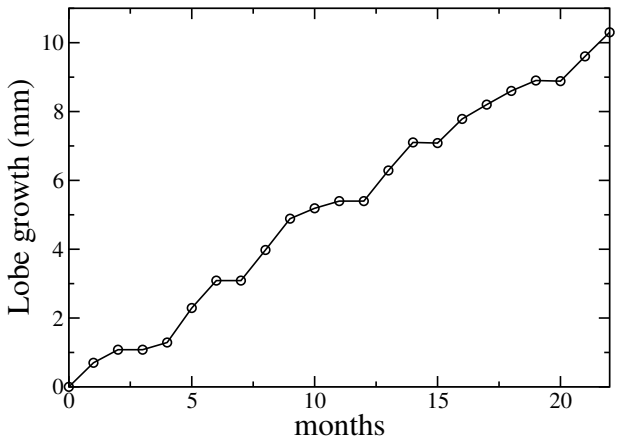

FIG. 13. Data from [3] plotted as a cumulative growth curve. The development of a single lobe of the foliose lichen *Parmelia conspersa* shows a cyclic pattern of radial growth over 22 months.

In agreement with the tight mycobiont control, the model has a well-controlled growth if $a\gamma_0 << 1$. This delegates the observed variability of the supercycle period T in Fig. 13 to that of θ_e. It has been indeed discussed that the mycobionts within the same *P. conspersa* lichen vary genetically by location. This would account for a non-uniform θ_e (see e.g. p.185 in [43] and [44]).

Within the mycobiont, the results suggest to focus on radial hyphal growth. A recent stereo-microscopic study of growth of a similar foliose lichen, *Xanthoparmelia farinosa*, showed that three months after inoculation the so-called "exploration hyphae" appear in large numbers, while at 6 months the hyphae are fully interlinked (anastomosed) [42]. Exploration hyphae participate in secreting an adhesive substance, which allows the lichen

to anchor to the substrate. A limited amount of the photobiont participates in this exploration, creating a spatial separation between the region where symbiotic metabolism is operating and the region where the adhesive substance is employed. Which part of this process represents the bottleneck that determines $\theta_e - \theta_0$ is difficult to say, as lichenologists question the life cycles of *P. conspersa*. Citing R. Honegger, "Can we assume that the mycobiont and photobiont cells making up the oldest, central parts of such thalli are decades or even centuries old, or is there a cell turnover in the entire thallus?" citehonegger1993developmental.

The duration of the spatial growth phase, $\theta_e - \theta_0 = 2.8$ mon, may just be the time it takes to reach the maximal sustainable spatial mismatch $\sim$ 2mm between the bionts, given the adhesion-limited speed $v = 0.8$ mm/mon. In the case of *X. farinosa* mentioned above the times were similar, while the spatial scales were smaller by a factor of 30. If the mechanism suggested here is confirmed, an extension of the model could also be applied to the 2D experiments on lobe division by R.A.Armstrong and coworkers (see [3] and references therein).

B. Crop yield cycles

In addition to alternate bearing of fruit trees [4], agricultural crops display multi-year yield cycles. For example, wheat in Yemen (Fig. 14(a)), had several cycles with $\theta_e = 6$ yrs, while barley in Ecuador (b) had cycles with $\theta_e = 7$ yrs. In terms of modeling, these historical data are available not for the spatial expansion $x(t)$, but for integrals of the type

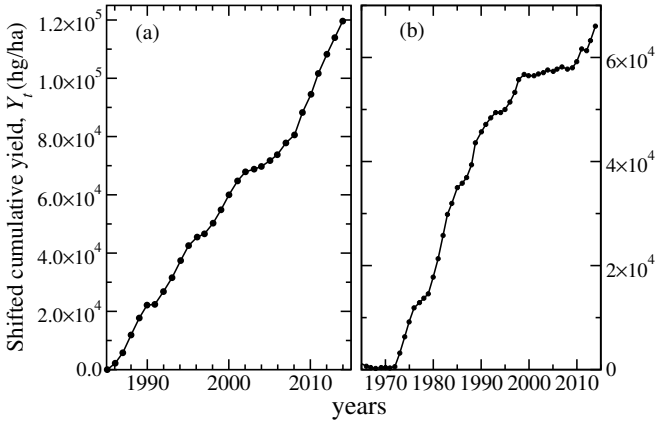

FIG. 14. Cumulative long-term records of annual crop yield, y_t of year t, summed up with a shift, $Y_t = \sum_{k=0}^{k=t}[y_k - \min(y)]$: (a) wheat in Yemen, (b) barley in Ecuador. Data from [5].

$$y_k = \int_{t_{k-1}}^{t_k} dt \int_{x_1(t)}^{x_0(t)} dx\, n(x,t), \tag{63}$$

taken over time windows of one year, $t_k = t_{k-1} + 1$. Such integrals may also exhibit cyclic behavior. During the years of low yields, the yields were not zero. In view of this, minimal annual yields were subtracted from the time series before additional summation in Fig. 14 (see caption).

Multi-year crop cycles are known since antiquity, and can in many cases be prevented by annual reseeding. Being perennial grasses, wheat and barley are always grown as annual crops. Yet, a multi-year memory can be seen in Fig. 14 in several countries. In these countries a small proportion of cultivated plants grows in the wild as perennials and so do their wild or previously used varieties. In wheat and barley, allogamous pollinators co-exist with self-pollinators, and therefore mature perennial plants of the same or close species growing in the wild might influence the agricultural yields. It is, in fact, known that Emmer wheat with its exceptional genetic diversity grows in Yemen [45], while Ecuadorean highlands have supported barley since 1800s [46]. A value of $T = 6$ to 7 yrs is similar to the perennial life span of grasses. A multi-year wild pollen analysis is required to support or refute this mechanism. In grasses as in many plants, the age diffusivity, $a \sim 0.1$ day, see Sec.II A, and γ_0 is of the order of hundreds per year, judging by the number of seeds a single annual plant may produce. Therefore $\gamma_0 \sim 0.01\,\mathrm{day}^{-1}$, so that the control is tight, $a\gamma_0 \ll 1$.

Since yield is connected to "spatial growth in the model by means of Eq. (63), the cycles are a sign of fast growth. Indeed, starting from small γ_0, and increasing it (as it happens with agricultural drive for higher yields), for a fixed *small* a, the system crosses the dashed line in Fig. 11 and develops cycles. The front speed $\bar{v}$ will eventually reach a maximum, as per bottom chart in Fig.12. While the model supports observations that the appearance of cycles is a response to rapid reproduction, a multi-year rapid reproduction (forced by annual reseeding) requires ample resources. If fact, the relation between cycles and strain is known in botany [4]. Prolonged strain makes the plants vulnerable to diseases. The cycles of barley yield were promptly followed by leaf rust, and yield deterioration in the late 1990s, as seen in Fig. 14(b) [47]. In the case of wheat, after emergence of multi-year cycles, the decline seen in Fig. 14(a) in mid 2000s was caused by the wheat stem rust pathogen, first identified in Uganda ([48], Fig.1). The subsequent yield rebounding was due to rapid introduction of engineered wheat varieties.

C. Swarming of locust *chortoicetes terminifera* in Eastern Australia

Swarming is associated with collective mobility and density-dependent phenotypes [49]. From the viewpoint of the present model, it is the considerable desynchronization of individual life cycles combined with high individual insect mobility that underlies our interest here, as it might shed light on why most insect swarms are recurrent but not periodic. Although insect swarms resemble organisms in some ways, we will argue that namely

the limitations of swarm collective control gives them an edge over tightly self-controlled species in the affected ecosystems.

The Australian Department of Agriculture and Water Resources has been collecting data on locust swarming (see [6] and references therein) since 1934, with evaluations complied every 4 months. The scales of outbreaks are defined semi-quantitatively, with scale 4 referring to a "plague, several hundred thousand hectares infested by bands/swarms in the agricultural zone" and scale 5 - a "major plague, over 500,000 hectares infested by bands/swarms in the agricultural zone". If we quantify the word "several" here as at least 2, then the transition from scale 4 to scale 5, corresponds to an increase in $\sim e$ times with spatial migration of several dozen kilometers. The data do show that if the current time step has scale 5, the previous step, on average had scale 4 and the step before that, had scale 3. Assuming that an increase of infested area in e times in 4 months, implies e times more locusts, we get $\gamma_0 = 1/4\,\text{mon}$, and probably bigger. If, instead, the data for the South American locust *Shistocerca cancellata* is used [26], with "mean reproductive rate and mean generation time" of 130 and 18 days, respectively, we find $\gamma_0 = \log(130)/18\ \text{day}^{-1} = 8\ \text{mo}^{-1}$. This was measured in laboratory conditions, in the absence of predators.

With the "field" value of γ_0, and using Eq. (62), one can estimate saturated spatial diffusivity, $D_0 \sim (50\text{km})^2/(2\cdot 4\text{mon}) \sim 300\,\text{km}^2/\text{mon}$, provided there is no dominant wind direction. The scales of outbreaks are usually logarithmic in nature, and we believe that a factor of e in area coverage could quantify the growth of infected areas. Then, it is possible to compute cumulative affected areas over time (arbitrarily arranged over the affected territory), see Fig. 15.

The age diffusion of locusts is considerable; we know that several generations can emerge during a favorable summer, so we estimate conservatively, $a \gtrsim 1$ mon. (Recall that in controlled laboratory conditions without predators the age diffusivities for *Schistocerca cancellata* are 7 days for females and 4 days for males.) The product $a\gamma_0$ is larger than with lichen and crops above, and according to the model, for such values of $a\gamma_0$, the supercycles may have periodicities larger than the life cycles of participating insects (Fig. 12), and the dependence of period T on $a\gamma_0$ is steep. The period is then *sensitive to noise*. For even larger values of $a\gamma_0$, linear growth dominates in the long term, but swarms still exhibit transient oscillations, see Sec.V B. This is similar to Fig. 15(a), where subsequent peaks of the autocorrelation function barely surpass their statistical errors, with the peak-peak lag of $T \simeq 3.8$ yr. Such lag exceeds the insect longevity [26] by an order of magnitude.

Further analysis using data in Fig. 15 shows that outbreak durations are close to adult insect longevities, $\sim$ 4 months. The inter-plague time windows are much larger. Combining these conditions with the above-mentioned period T sensitivity to noise, we conclude that the swarms may appear unpredictable, thus providing an edge over ecosystem control and agricultural control.

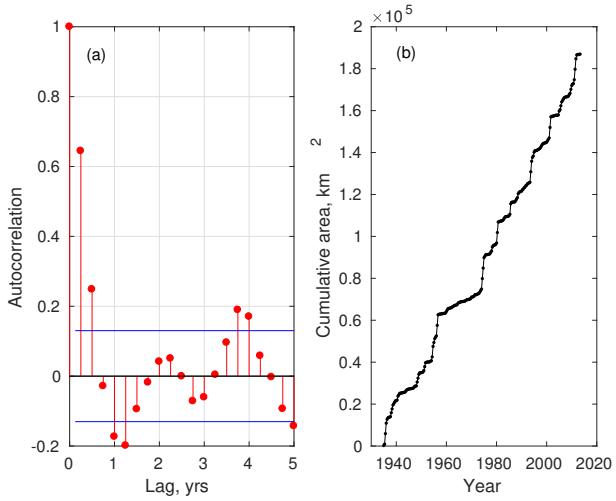

FIG. 15. Autocorrelation of locust outbreak scales (a). The horizontal lines display the confidence interval. Estimated cumulative area occupied by locusts outbreaks (b) using data from [6] and a conversion convention based on factor e: scale 5 is $5000\,\text{km}^2$, scale 4 is $5000/e\,\text{km}^2$, scale 3 is $5000/e^2\,\text{km}^2$, etc.

According to the Australian Department of Agriculture, "Heavy summer rainfalls in western Queensland often lead to large population increases and subsequent southward migrations in late summer and autumn. This pattern has characterized several of the recorded major pest outbreaks, or plagues." Large increase in foliage following rainfalls is suggested here as an external trigger or driver, despite the fact that this driver by itself does not possess the observed multi-year autocorrelation structure with $T = 3.8$ yrs.

Since the seventies, the intervals between the largest scale-5 plagues are clustered around values from 5 to 10 years, while before that they were typically twice as large. (Such long-term trend is also consistent with the history of North American locust plagues in 19 and 20th centuries, due to the growth of agricultural land use [50].) It could be that with the growth of the agricultural use of land promoting annual crops, the locust community does not have to wait as long as it used to for vegetation to rebound, and outbreaks can reemerge sooner. One can see in Fig. 15, the average slope of the cumulative curve is somewhat higher since the seventies. It could be that the observed lag of 3.8 years is the time required for sufficient restoration of combined biomass of foliage available to locusts, an evolving combination of both wild and cultivated plants.

VII. CONCLUSION

A model has been introduced which may improve understanding of the cyclic growth of multicellular organ-

isms, to facilitate quantitative studies and indicate connection with previous models of non-linear spatial transport, such as models used in insect dispersal and the KPPF equation. The present model, making use of known processes for physiological aging along the variable θ and spatial transport along x, allowed us to see in more detail how collective cycles emerge.

It has been shown that a cellular birth and death process, characterized by stochastic physiological aging with age diffusivity a, in presence of Malthusian growth γ_0 and nonlinear spatial diffusion with an age-limited motility, may produce stable cyclical expansions for a range of parameters. We have found that the product $a\gamma_0$ is one of the key quantities for observing cyclical waves with windows of boost and consolidation. When $a\gamma_0 \lesssim 0.1$ is small enough, while Malthusian growth is rapid enough, collective cycles become the asymptotic behavior with periods shorter than cell lifetimes. For intermediate $a\gamma_0$, we find that the supercycle period could well exceed cell lifetimes, while spatial expansion rates reach a maximum. For large $a\gamma_0$ linear spatial growth prevails. The fastest spatial expansion occurs in the supercycling regime.

A key development on the theoretical side has been deriving the equations for the mobile fronts using the parametrically driven similarity approximation. It is based on the assumption of fast diffusion and slow hull expansion of the density profiles, at parameters $m \gg 1$ of the nonlinear spatial diffusivity. It simplifies the analysis, by reducing the study of a non-linear PDE for the population density $n(t, \theta, x)$ to solving an ODE system for the location of the moving fronts. The essence of this approximation is to evolve the population through a set of similarity solutions, by properly adjusting the solution parameters in time. The approximation has been tested in several exact cases, for which the solution is available. We have supplemented the theoretical analysis of the model PDE with direct numerical simulations to illustrate the population dynamics and the emergence of cycles as compared with the analytical solution derived under the assumption of the parametrically driven similarity approximation. By means of both tools, we have analyzed the first cycle which is found to be special. This matches the behavior of *Proteus mirabilis* which colonies on hard agar have a distinct first terrace, the emergence of cotyledons in plants, and others.

Three potential applications were selected. In all cases, the observed cycles are of rather intriguing origin, and point to collective long-term development of communities of multicellular organisms. For tightly held "communities" such as lichen and crops, the cycle phases match the mycobiont time scales (lichens) or perennial species growing nearby in the wild (crops). For loosely held communities with variable density, such as locust swarms, we argue that the expansion phase is clearly limited by insects. The consolidation phases may be determined by both insects (as per the model in the given parameter range) and by plants, and only tuned by weather.

A version of this model was previously applied to *Proteus mirabilis* bacteria colonies [17, 18], which tend to form recurrent terraces on hard agar with surprisingly robust periodicity [33]. It might also be applicable to tightly controlled phenomena in marine plankton, e.g. to diurnal rhythm of luminescence of the dinoflagellate *Gonyaulax polyedra*, which persists under conditions of constant low light and constant temperature for many days [51], eventually losing correlation with the time of the day. An opposite extreme example of very elastic cycles, is the reappearance of mosquitoes, which could reproduce in just a few weeks or in more than a year, depending on conditions [52]. Multi-annual oscillations have been observed in large-scale populations of many seabirds [53–55] in absence of any apparent prey-predator mechanisms and belong to the cases of intermediate control.

Two properties of supercycles stand out in terms of biological significance: (i) these cycles are responsible for a faster spatial expansion rate for a given biomass growth rate as compared to linear growth, and (ii) these cycles can entrain and organize a spectrum of (asynchronous) life cycles of participating cells or organisms.

Finally, here Malthusian dynamics has been assumed as representative of early growth mechanisms, which also facilitated the analytical treatment. Other growth models might be implemented, like the logistic model. We can anticipate that in such case, if the logistic saturated concentration exceeds n_0 where the spatial diffusivity peaks, the presented behavior will survive. If the saturation occurs earlier, it will prevent consolidation, and a linear regime will emerge. Jointly, this offers a different route to switch supercycles on and off, and could be studied in more detail.

ACKNOWLEDGMENTS

This study has been supported, in part, by the Spanish Ministry of Economy and Competitiveness under grant DPI2016-75791-C2-1-P and, in part, by Quant Isle Ltd.

Appendix A: Solution of the age-independent problem for time dependent growth rates $\gamma(t)$

With unrestricted non-linear diffusivity, Eq.(8) may be integrated for an arbitrary growth rate $\gamma(t)$. Indeed, a transformation $\mathfrak{n}(x,t) = h(t)y(x,\tau(t))$, results in

$$h'y + h\tau'\frac{\partial y}{\partial \tau} = D_0 n_0^{-m} h^{m+1}\frac{\partial}{\partial x}\left(y^m\frac{\partial y}{\partial x}\right) + \gamma h y. \quad \text{(A1)}$$

Such transformation is motivated by the fact that the exact solution of Eq. (8) without the growth term $\gamma\mathfrak{n}$ is known [14]. If one chooses the scaling function $h(t)$ to be $h' = \gamma h$, $\tau' = h^m$, the non-linear diffusion problem is

recovered, but now without the growth term:

$$\tau = \int_{t_0}^{t} h^m(t_1)dt_1, \quad \log h = \int_{t_0}^{t} \gamma(t_1)dt_1, \quad \text{(A2)}$$

$$\frac{\partial y}{\partial \tau} = D_0 n_0^{-m} \frac{\partial}{\partial x}\left(y^m \frac{\partial y}{\partial x}\right). \quad \text{(A3)}$$

Here, t_0 is an arbitrary initial time, when the initial concentration profile has been forgotten. Integrating Eq. (A3) over the x-axis, one can see that the integral $\int y(x,\tau)\,dx$ is conserved, this is the normalization condition. We are interested in localized solutions of Eq. (A3). One can easily check that Eq. (A3) is invariant with respect to a transformation, where τ is scaled in k times, the space axis x is magnified in $k^{1/(m+2)}$ times and the solution y is rescaled in $k^{1/(m+2)}$ times (Eq. ((A3)) has four different types of transformations which leave it invariant [37]). A self-similar solution of the form

$$y(x,\tau) = \frac{Ag(z)}{x_0(\tau)}, \quad z = \frac{x}{x_0(\tau)}, \quad \text{(A4)}$$

is appropriate, where A is the normalization constant. The integral $\int y(x,\tau)dx = A\int g(z)dz$ does not depend on the transformed time τ. Substituting Eq. (A4) into Eq. (A3) and dividing the resulting equation by $A/x_0(\tau)$, one finds

$$-\frac{x_0'}{x_0}(g + zg') = \frac{D_0 A^m}{n_0^m x_0^{m+2}}(g^m g')'. \quad \text{(A5)}$$

For this equality to hold at any τ and z one must require

$$\frac{x_0'}{x_0} = \frac{1}{c}\frac{D_0 A^m}{n_0^m x_0^{m+2}}, \quad \text{(A6)}$$

$$g + zg' + c(g^m g')' = 0, \quad \text{(A7)}$$

where c is a constant. The solution of Eq. (A7) defines the similarity function. This equation explicitly contains z, and does not possess translational invariance. For a diffusion problem, translational invariance is broken by a localized initial condition. The evolution of such condition is described by this similarity solution. Integrating this ODE once, we obtain $zg + cg^m g' = 0$. The constant of integration has been set to zero since a localized solution is being sought, and the left-hand side must vanish at both infinities in space. Integrating again, we have $g^m = m(C - z^2)/2c$. For convenience, one can fix scale and amplitude, $g(0) = 1$, $g(1) = 0$. Scale and amplitude are governed by x_0 and A, respectively, and any different choice here will be compensated back by A and x_0. Then the solution is $g(z) = (1 - z^2)^{1/m}$, and $c = m/2$. Equation (A6) is consistent if

$$x_0(\tau) = \left[\frac{2(m+2)D_0 A^m \tau}{m n_0^m}\right]^{1/(m+2)}, \quad \text{(A8)}$$

where the constant of integration was chosen so that $x_0(0) = 0$ for the localized initial condition. Integrating Eq. (8) over x, and introducing the total number of cells $\mathfrak{N}(t)$,

$$\mathfrak{N}(t) = \int \mathfrak{n}(x,t)dx, \quad \text{(A9)}$$

we obtain $\mathfrak{N}' = \gamma\mathfrak{N}$, or $\mathfrak{N}(t) = 2N_0 h(t)$, with $h(t)$ given by Eq. (A2). Here the initial total number of particles is $2N_0$, or N_0 for each half-axis. This choice of normalization is needed for what follows in subsequent sections.

Appendix B: Wave traveling with a constant speed

The details on the numerical integration of Eq. (34) are as follows. Positioning the leading front of the wave at $z = 0$, and integrating Eq. (34) over the domain, from $z = 0$ on the leading front where $\eta = 0$, to some $z = z_0$ at the trailing front defined by $\mathfrak{n} = n_0$ or $\eta(z_0) = 1$, we get a solvability condition, reflecting conservation of cells,

$$\kappa = \left[\int_0^{z_0} \eta(z)\,dz\right]^{-1}. \quad \text{(B1)}$$

where use has been made of the condition that the diffusion flux $f\eta'$ vanishes on both fronts. Equation (B1) ensures that the total growth per unit time ($\kappa\int dx\eta$ in dimensionless units) is equal to the cell deposition rate at the trailing front, which is moving with the speed 1 at concentration 1 in these units. In dimensional units, the selected speed is $v = (\gamma_0 D_0/\kappa)^{1/2}$.

Equation (34) can be converted into a first-order ODE, by introducing a new function $w(\eta) = f\eta'$, and assuming η to be the new independent variable. The function w is the diffusive flux in dimensionless units, which satisfies

$$ww' + w = -\kappa\eta f. \quad \text{(B2)}$$

This is an Abel equation of the second kind, and its analytical solution for our right-hand side term is unknown. However it can be solved numerically, and defines a function $\kappa(m)$, and front width $x_0 - x_1$, given an overdetermined set of four boundary conditions. At small z, in the vicinity of the leading front, the solution could be approximated by $\eta(z) = (mz)^{1/m}$, which satisfies, $\eta' = (f\eta')'$, i.e. (34) without the source term. For a second-order ODE this implies two boundary conditions at small z. In the course of the numerical integration, one stops at a point $z = z_0$ where $\eta'(z_0) = 0$, and requires $\eta(z_0) = 1$. This point is the trailing front.

Appendix C: Slowing wave

Here $\gamma(t) = \beta/t$, $\beta > 0$. We start with unrestricted diffusion, in which case Eq. (A2) gives

$$h(t) = \left(\frac{t}{t_0}\right)^{\beta}, \quad \tau(t) = \frac{t_0}{m\beta + 1}\left(\frac{t}{t_0}\right)^{m\beta+1}, \quad \text{(C1)}$$

while $x_0(t_1) \propto t_1^{1/(m+2)}$. The formulae for the population size and the concentration read,

$$x_0(t) = \left[\frac{2^{m+1}(m+2)D_0 N_0^m t_0}{m(m\beta+1)(n_0 b)^m}\right]^{\frac{1}{m+2}} \left(\frac{t}{t_0}\right)^{\frac{m\beta+1}{m+2}}, \quad \text{(C2)}$$

and

$$\mathfrak{n}(0,t) = n_0 \left[\frac{2m(m\beta+1)N_0^2}{(m+2)D_0 t_0 (n_0 b)^2}\right]^{\frac{1}{m+2}} \left(\frac{t}{t_0}\right)^{\frac{2\beta-1}{m+2}}. \quad \text{(C3)}$$

Again, this is a two-parameter (N_0, t_0)-family of similarity solutions of sub-exponential expansion. The evolution of the maximal concentration now depends on the growth rate amplitude, β. At $\beta < 1/2$ the concentration diminishes, while the population size grows faster than pure non-linear diffusion without growth. Its exponent is lesser than the value 1/2 of linear diffusion. At $\beta = 1/2$ one finds a special boundary case, when the maximal concentration is time-independent, while the population size grows as a square-root of time, $x_0(t) \propto (t/t_0)^{1/2}$. At $\beta > 1/2$, the maximal concentration grows, while the population size exponent, $(m\beta+1)/(m+2)$ spans the interval $[1/2, \beta]$ as $0 \le m \le \infty$. Only in the latter case, immobilization may occur if a diffusivity cutoff at $\mathfrak{n} = n_0$ is introduced.

When the diffusivity cutoff is introduced, the transformations applied to Eq. (8) mentioned in Sec. IV C 2 lead to Eq. (40), which again does not have an analytical solution. This time it is not reducible to an Abel equation anymore, but two interesting facts should be mentioned. First, all lengths in the problem scale like $t^{1/2}$, including the positions of the leading and trailing fronts, and the width of the wave. The super-diffusional exponent $(m\beta+1)/(m+2)$ in Eq. (C2) does not survive when the diffusivity cutoff is introduced: the problem effectively migrated to a $\beta = 1/2$ expansion scenario, despite the fact that a source growth rate with multiplier $\beta > 1/2$ is maintained. This is clearly the action of the trailing front and cross-influence of the two fronts. Second, there is no translational invariance, as we cannot eliminate u by a z-shift, and still keep the leading front position at $z = 0$. Thus u remains, and gets adjusted, to solve for the boundary value problem, $g(z) = (muz/2)^{1/m}$ for small z, with $g(z_0) = 1$, $g'(z_0) = 0$ for some $z_0 > 0$, providing selection for the front width and its velocity.

[1] S. N. Semenov, L. J. Kraft, A. Ainla, M. Zhao, M. Baghbanzadeh, V. E. Campbell, K. Kang, J. M. Fox, and G. M. Whitesides, Nature **537**, 656 (2016).
[2] A. F. Taylor, Nature **537**, 627 (2016).
[3] R. A. Armstrong, Symbiosis **47**, 9 (2009).
[4] S.P. Monselise and E.E. Goldschmidt, Hortic Rev **4**, 128 (1982).
[5] FAOSTAT, "Food and Agriculture Organization of The United Nations, Statistics Division, Accessed on May 25, 2016, http://faostat3.fao.org/download/Q/QC/E," (2016).
[6] Department of Agriculture, "History of locust and grasshopper outbreaks in Australia, Accessed on November 18, 2014, http://www.agriculture.gov.au/animal-plant-health/locusts/about/history," (2014).
[7] E. Méhes and T. Vicsek, Integrative biology **6**, 831 (2014).
[8] J. A. Sherratt and M. J. Smith, Journal of The Royal Society Interface **5**, 483 (2008).
[9] R. A. Fisher, Ann. Eugenics **7**, 355 (1937).
[10] A. K. I. Petrovsky, and N.Piskunov, Bull. Univ. Moscou, Ser. Internat., Sec. A **1**, 1 (1937).
[11] M. A. Fuentes, M. N. Kuperman, and V. M. Kenkre, Phys. Rev. Lett. **91**, 158104 (2003).
[12] E. H. Colombo and C. Anteneodo, Phys. Rev. E **86**, 036215 (2012).
[13] R. C. MacCamy, Journal of Differential Equations **39**, 52 (1981).
[14] J. D. Murray, *Mathematical Biology* (Springer, Berlin, 1993).
[15] E. Ben-Jacob, I. Cohen, I. Golding, and Y. Kozlovsky, in *Mathematical Models for Biological Pattern Formation*, IMA Volumes in Mathematics and its Applications, Vol. 121, edited by P. Maini and H. Othmer (Springer New York, 2001) pp. 211–253.
[16] J. VanSickle, Journal of theoretical Biology **64**, 571 (1977).
[17] S. Esipov and J. A. Shapiro, J. Math. Biology **36**, 249 (1998).
[18] S. Esipov, in *Coherent Structures in Complex Systems*, Lecture Notes in Physics, Vol. 567, edited by D. Reguera, J. M. Rubí, and L. L. Bonilla (Springer Berlin Heidelberg, 2001) pp. 242–251.
[19] G. Barenblatt, *Scaling, Self-Similarity and Intermediate Asymptotics* (Cambridge University Press, 1996).
[20] R. Calendar, ed., *The Bacteriofages* (Oxford University Press, New York, 2005).
[21] N. Dimmock, A. J. Easton, and K. N. Leppard, *Introduction to Modern Virology, 5th Ed.* (Blackwell Publishing, Malden, MA, 2007).
[22] E. O. Wilson, Science **166**, 592 (1969).
[23] J. Oteros, H. García-Mozo, L. Vázquez, A. Mestre, E. Domínquez-Vilches, and C. Galán, Agriculture, Ecosystems and Environment **179**, 62 (2013).
[24] R. B. Primack, Journal of Ecology **68**, 849 (1980).
[25] J. H. Zhao, X. G. Kang, H. D. Zhang, and L. Liu, Ying Yong Sheng Tai Xue Bao. (in Chinese) **20**, 1832 (2009).
[26] N. E. Sanchez, E. Wittenstein, M. L. de Wysiecki, and C. E. Lange, Journal of Orthoptera Research , 121 (1997).
[27] C. Gardiner, *Handbook of Stochastic Methods for Physics, Chemistry and the Natural Sciences* (Springer, Berlin, 1985).
[28] R. A. Holland, M. Wikelski, and D. S. Wilcove, Science **313**, 794 (2006).
[29] J. Buhl, G. A. Sword, F. J. Clissold, and S. J. Simpson, Behavioral Ecology and Sociobiology **65**, 265 (2011).
[30] G. Ariel and A. Ayali, PLoS Comput Biol **11**, e1004522 (2015).

[31] E. F. Keller and L. A. Segel, Journal of theoretical biology **30**, 225 (1971).

[32] A few words should be said about the periodic boundary condition at θ_e. To avoid age diffusion acting as a "birth-death" agent, it is possible to put a sink term at θ_e and a source term at θ_0, and match their fluxes to make sure that nothing is born backwards. Regarding the differences in behavior of the two models, with and without such a construct, we can state that there are no differences as long as we focus on scales exceeding the age-diffusion length over the time to overcome this distance due to the drift.

[33] O. Rauprich, M. Matsushita, C. J. Weijer, F. Siegert, S. E. Esipov, and J. A. Shapiro, Journal of Bacteriology **178**, 6525 (1996).

[34] H. Dingle, *Migration: the biology of life on the move* (Oxford University Press, USA, 2014).

[35] See Supplemental Material at (URL will be inserted by publisher) for the implementation of the model solver in MATLAB.

[36] W. van Saarloos, Phys. Rev. A **37**, 211 (1988).

[37] T. Witelski and A. Bernoff, Studies in Applied Mathematics **100**, 153 (1998).

[38] J. Vazquez, Transactions of the American Mathematical Society **277**, 507 (1983).

[39] L. Landau and E. "Lifshitz, *Mechanics, Third Edition: Volume 1 (Course of Theoretical Physics)* (Elsevier, 1976).

[40] D. Hill, Symbiosis **14**, 325 (1992).

[41] W. B. Sanders, American journal of botany **101**, 1836 (2014).

[42] R. A. García and V. G. Rosato, Mycology , 1 (2017).

[43] T. H. Nash, *Lichen biology* (Cambridge University Press, 1996).

[44] M. R. Mansournia, W. Bingyun, N. Matsushita, and T. Hogetsu, The Lichenologist **44**, 419 (2012).

[45] E. D. Badaeva, J. Keilwagen, H. Knüpffer, L. Waßermann, O. S. Dedkova, O. P. Mitrofanova, O. N. Kovaleva, O. A. Liapunova, V. A. Pukhalskiy, H. Özkan, *et al.*, PloS One **10**, e0128556 (2015).

[46] R. W. Jamieson and M. B. Sayre, Journal of Anthropological Archaeology **29**, 208 (2010).

[47] E. Villacrés, M. Rivadeneira, *et al.*, Food Barley: Importance, Uses and Local Knowledge , 127 (2005).

[48] R. P. Singh, D. P. Hodson, J. Huerta-Espino, Y. Jin, P. Njau, R. Wanyera, S. A. Herrera-Foessel, and R. W. Ward, Advances in Agronomy **98**, 271 (2008).

[49] C. Lomer, R. Bateman, D. Johnson, J. Langewald, and M. Thomas, Annual review of entomology **46**, 667 (2001).

[50] C.K. Yoon, "Looking Back at the Days of the Locust," (2002).

[51] J. W. Hastings and B. M. Sweeney, The Biological Bulletin **115**, 440 (1958).

[52] F. Soper, Bulletin World Health Organization **36**, 536 (1967).

[53] J. I. Hodges, J. G. King, B. Conant, and H. A. Hanson, *Aerial surveys of waterbirds in Alaska 1957-94: population trends and observer variability*, Tech. Rep. (DTIC Document, 1996).

[54] A. J. Gaston and A. Powell, The Auk **120**, 362 (2003).

[55] C. Egevang and M. Frederiksen, Waterbirds **34**, 107 (2011).

[56] R. Honegger, New Phytologist **125**, 659 (1993).

[57] M. Menaker, L. Moreira, and G. Tosini, Brazilian Journal of Medical and Biological Research **30**, 305 (1997).

[58] C. A. Czeisler, J. F. Duffy, T. L. Shanahan, E. N. Brown, J. F. Mitchell, D. W. Rimmer, J. M. Ronda, E. J. Silva, J. S. Allan, J. S. Emens, *et al.*, Science **284**, 2177 (1999).

[59] H. M. Stauss, American Journal of Physiology-Regulatory, Integrative and Comparative Physiology **285**, R927 (2003).

[60] T. R. Soderstrom and C. E. Calderon, Biotropica , 161 (1979).

[61] D. H. Janzen, Annual Review of Ecology and Systematics , 347 (1976).

[62] A. J. Phillips, C. A. Czeisler, and E. B. Klerman, Journal of biological rhythms **26**, 441 (2011).

[63] A. H. Tsang, J. L. Barclay, and H. Oster, Journal of molecular endocrinology **52**, R1 (2014).

[64] J. A. Carrillo, M. Fornasier, G. Toscani, and F. Vecil, in *Mathematical Modeling of Collective Behavior in Socio-Economic and Life Sciences*, Modeling and Simulation in Science, Engineering and Technology, edited by G. Naldi, L. Pareschi, and G. Toscani (Birkhuser Boston, 2010) pp. 297–336.

[65] W.-M. Ni, Notices Amer. Math. Soc. , 9 (1998).

[66] For a constant negative rate, $\gamma = \gamma_0$, $\gamma_0 < 0$, this transformation is mentioned in chapter 9, page 253, problem 4 in Ref. 14.